Virginia Commonwealth University

VCU Scholars Compass

2012

Mechanical Characterization of Patterned Silver Columnar Nanorods with the Atomic Force Microscope.

Sean Kenny
Virginia Commonwealth University

Mechanical Characterization of Patterned Columnar Silver Nanorods with the Atomic Force Microscope

A thesis submitted in partial fulfillment of the requirements for the degree of Master of Science in Physics / Applied Physics at Virginia Commonwealth University.

By

Sean Kenny

B.S. in Physics

Longwood University, 2009

M.S. in Physics/Applied Physics

Virginia Commonwealth University, 2012

Major Director:

Dexian Ye, Ph.D, Assistant Professor, Department of Physics

Virginia Commonwealth University

Richmond, Virginia, 23284

April 30th, 2012

Table of Contents

List of Figures

List of Tables

Abstract

Mechanical Characterization of Patterned Silver Columnar Nanorods with the Atomic Force Microscope

By Sean M. Kenny

A thesis submitted in partial fulfillment of the requirements for the degree of Master of

Science at Virginia Commonwealth University

Virginia Commonwealth University, 2012.

Director: Dr. Dexian Ye, Assistant Professor Department of Physics

Patterned silver (Ag) columnar nanorods were prepared by the glancing angle physical vapor deposition method. The Ag columnar nanorods were grown on a Si (100) substrate patterned with posts in a square "lattice" of length 1 μm. An electron beam source was used as the evaporation method, creating the deposition flux which was oriented 85° from the substrate normal. A Dimension Icon with NanoScope V controller atomic force microscope was used to measure the spring constant in 10 nm increments along the long axis of five 670 nm long Ag nanorod specimens. The simple beam bending model was used to analyze the data. Unexpected behavior of the spring constant data was observed which prevented a conclusive physically realistic value of the Young's modulus to be calculated.

Chapter 1: Introduction

1.1 Motivation

Nanofibers and nanorods have been used in a wide array of applications, ranging from tissue engineering,[1] reinforcement in composites,[2] and micro/nano-electromechanical systems (MEMS/NEMS).[3] While these nanomechanical devices are in use, the forces present in their applications can result in both elastic and plastic deformation, along with mechanical failure. Development of future nanomechanical devices requires characterization of properties of these nanocolumnar arrays, in order to realize their practical applications.[4]

Here three main techniques are reviewed which are found in literature for atomic force microscope (AFM) based mechanical characterization of nanorods: the nano tensile test, the nanomechanical bending test, and nanoindentation.[5] As with a macroscopic stress-strain experiment, the nano tensile test requires tension to be exerted along the long axis of the nanorods in a uniform fashion, and direct measurement of the resulting stress and strain in order to extract the Young's modulus. The AFM cantilever is used to apply the force, and the nanorod must be fixed to one end of the cantilever while the other end of the nanorod is fixed to the substrate. Due to the experimental difficulties of realizing this setup on a nanoscale, the nano tensile test is reported as the most difficult to perform.[5, 6] Other difficulties inherent to this test include alignment and gripping, since direct manipulation of the testing specimen is required [5]. The geometry of the silver nanorods studied in this thesis is not well-suited for the tensile test, as will be discussed in Section 1.4.

The nanoindentation method is reported by Tan and Lim to be the most convenient, however the application of this test requires not only that the nanorod specimen lay flat on a rigid substrate, but a reliable method for measurement of both the indentation depth and applied force exist, and also sufficient adhesion between the substrate and nanomaterial exist.[5] The AFM cantilever is either assumed infinitely rigid, or not. If the cantilever deformation is not neglected, convolution of the cantilever deformation during the test makes extraction of the Young's modulus of the sample more complicated.[5] The nanorods studied in this thesis are also not intrinsically suited for this test; since the nanorods exhibit cantilevered-beam geometry, any nanoindentation force applied will result in a bending moment and therefore convolution between the measurement of the applied nanoindentation force and the restoring force resulting from the bending of the cantilevered-style beam.

This thesis seeks to investigate the application of the *ex situ* nanomechanical bending test to extract the spring constant and Young's modulus of silver (Ag) nanorods. The nanomechanical bending test is reported as giving the most data spread of all the methods discussed,[7] however this test is well-suited for the sample geometry of the Ag nanorods which is discussed in Section 1.4. The method described first by Wong *et al.* in 1997[8] is the experimental procedure used in this thesis, however using force-distance spectroscopy in place of lateral force microscopy to extract the spring constant of the nanorods.

Other applications of the bending test employing an AFM is reported in studies by Gaire *et al.* in 2005.[9] Gaire *et al.* reports measuring the stiffness of amorphous silicon nanorods grown by the glancing angle deposition (GLAD) technique using an AFM and plotting the stiffness versus a geometrical factor common to all of the nanorods, the slope of which is the Young's modulus. Their results indicate the scatter common to the bending test, with a value of 94.14 ±

10.21 GPa. A similar experimental procedure was followed by Nagar *et al.* in 2009,[10] where they report a spring constant of 65.6 ± 20.8 Nm^{-1} for similarly prepared slanted silicon nanorods, which also demonstrates the scatter common to the bending test.

The method of Wong *et al.*[8] is to measure the spring constant of nanorod specimens using the AFM at incremental distances along the long axis. The spring constant data are then plotted versus the positive distance from the pinning point, and the Young's modulus is extracted by fitting the curve to the simple beam bending model discussed in the next section. Wong *et al.*[8] argue that by measuring the force constant in this manner, a more reliable measurement of the Young's modulus is made and the scatter in the measured spring constant data becomes less relevant.

1.2 Atomic Force Microscopy and Nanomechanical Characterization

The AFM-was developed by Binnig, Quate and Gerber in 1985.[11] Since its development the AFM has made a large contribution in the field of nanomechanics, owing to its ability to measure pico- to nano-Newton forces.[12] Due to the nature of the AFM, a topographical image of the sample must first be obtained in order to locate nanostructures for mechanical testing.

The two main imaging modes of the AFM are contact mode (static AFM) and tapping mode (dynamic AFM). The basic principle of static AFM operation is simple: the tip of a micro machined cantilever, commonly made of single crystal silicon Si, is scanned by a piezoelectric scanner in a raster pattern in the x-y plane while in contact with the sample surface. Generally the x direction is referred to as the fast-scan direction, and y the slow-scan direction. The

piezoelectric scanning tube along with the raster pattern followed during both static and dynamic AFM imaging modes is shown in **Figure 1**.

Due to sample-cantilever interaction, the cantilever can deflect both normally with respect to the surface (z direction) of the sample and torsionally along the long axis of the cantilever. One side of the AFM cantilever may be coated with a thin coating of reflective metal, typically aluminum, so that a laser spot when aligned on the end of the cantilever so the beam is reflected back to a photosensor diode can measure the deflection of the cantilever. This is referred to as the optical-lever scheme. The deflection of the cantilever is measured by the change in voltage signal of the four-quadrant photo sensor diode. The AFM software, employing a feedback loop, keeps the deflection of the cantilever, and therefore the force exerted by the cantilever on the surface, constant. The topographical features of the surface are then represented by the voltage supplied by the feedback loop to the piezoelectric scanner located at the base of the cantilever in order to keep the normal deflection of the cantilever constant. An overall schematic of the AFM is presented in **Figure 2**.

In dynamic AFM the cantilever is not held fixed but is vibrated at its fundamental resonance frequency. The feedback loop then monitors the mean squared amplitude of vibration of the cantilever which is held fixed. Sample features are again represented by the change in voltage required to move the AFM cantilever in the normal direction in order to keep the mean squared vibrational amplitude constant.

The deflection of the cantilever is of course caused by interaction with the surface of the sample. The forces responsible for the deflection of cantilever can be either attractive or repulsive. Attractive forces will include van der Waals (vdW) interactions, capillary forces, electrostatic forces and chemical forces, while repulsive forces include Pauli-exclusion

interaction and Coulombic interaction [12]. The Lennard-Jones (LJ) 6-12 potential has both of these attractive and repulsive forces built in and has the form,[13]

$$\Phi(r) = \frac{-1}{r^6} + \frac{1}{r^{12}} , \qquad (1.1)$$

where r is the distance between the cantilever tip and the sample. The repulsive force is the positive term while the attractive force is the negative term. A plot of the LJ potential is found in **Figure 3.**

The imaging modes above are standard imaging modes, while the imaging mode used in data collection in this thesis was the Bruker proprietary QNM PeakForce[14] imaging mode. In order to understand the concepts of this imaging mode, first a digression into force-distance spectroscopy is necessary.

In force-distance spectroscopy the x-y motion of the piezoelectric scanner is halted and the cantilever is "ramped" in the z direction while the deflection of the cantilever is monitored by the optical lever scheme. The distance the cantilever is ramped is defined by the user, and the sample-cantilever interaction force in the elastic deformation regime can be described by Hooke's Law,

$$F_c = -k_c \delta_c , \qquad (1.2)$$

where F_c is the force exerted by the cantilever on the surface, k_c is the cantilever spring constant and δ_c is the deflection of the cantilever from the equilibrium position. The cantilever can be modeled by Hooke's law when the cantilever deflection is kept small so as to keep the deformation in the elastic regime; that is to not permanently deform the cantilever. The deflection of the cantilever is then plotted as a function of the z-piezo ramp distance, and the spectra is called a force curve.

There are several key features force curves exhibit. A force curve is shown in **Figure 4**. First, as the z piezo moves the cantilever from region 1 to region 2 the cantilever is not deflected. The data above show a baseline deflection that has a negative slope indicating a long-range attractive force which is attributed to static charge on the sample surface inducing an image charge on the AFM cantilever. At point 2, the van der Waals force and capillary force due to the adsorbed water layer on the sample cause a sudden negative deflection of the cantilever. This is called the "jump to contact" point. Beginning at point 3 the tip is in physical contact with the sample surface. The rest of the extension ramp is completed then the retract cycle begins at point 4. At point 5 the cantilever restoring force overcomes the capillary force and the "jump off contact" point is reached. The difference between the force at point 6 and the minimum at point 5 can be taken as the force of adhesion; here this force was about 40nN. The z piezo then retracts the rest of the way from point 6 to point 7 and the ramp cycle is complete.

The Bruker PeakForce Quantitative Nanomechanical Mapping (QNM) Package[14] can be thought of as a hybrid imaging mode that combines contact mode and tapping mode; the AFM takes a fast force curve at each pixel in the scan, keeping the tip-sample force below a preset setpoint, and then lifts the cantilever and moves to the next point in the scan. This is especially advantageous when imaging a sample with nanorods since during imaging this force and therefore the sample deformation can be minimized resulting in an artifact-free image. An extension of this package, called ScanAssyst[14], uses algorithms developed by Bruker to change scanning parameters in real-time using the QNM[14] force curve data resulting in near artifact-free images.

During preliminary studies, it was found that the standard imaging modes exhibit artifacts in the image due to the nanorod bending during scanning. An image recorded in standard tapping

mode with discontinuities in the slow scan direction as well as artifacts in the topological profile is shown below in **Figure 5** b, with a comparison of an image taken with the proprietary PeakForce QNM package[14] (**Figure 5** a) that exhibits almost no artifacts due to the minimization of the tip-sample force during imaging.

1.3 Hooke's Law, Elastic Theory and Beam Bending

Robert Hooke in 1678 laid the foundation for modern elastic theory with his publication of his work with metal springs titled, "The power of any spring is in the same proportion with the Tension Thereof."[15] This work was actually first published by Hooke in 1676 as the anagram, "*ceiiinosssttuu*" at the end of another published work [16], as was a common practice at the time in order to stake a claim to a discovery. The anagram decoded reads in Latin, "*ut tension sic vis*," which translates to "as the extension, so the force."[17] This relationship can be described mathematically by the well-known formula of the same form of **Equation (1.2),**

$$F = -k\Delta x, \tag{1.3}$$

where F is the restoring force exerted by the spring with a spring constant k displaced from its equilibrium by Δx. An important condition is that this is only valid when the relationship between stress and strain is linear, as is the case for small deformations in most isotropic homogenous materials. When the relationship between stress and strain is linear in a material for a given displacement, the material is said to be linearly elastic. This relationship does not only hold for mechanical springs, but also is applicable to the deformation of beams for small displacements, as will be visited after a discussion of linear elastic theory.

It is quite apparent that when external forces are applied to a body or material deformations can result. When these external forces are removed, however, if the body returns to its original

state after the external force or forces are removed the body is said to be perfectly elastic.[18] The generalized theory of elasticity, when defining stress and strain, makes reference to two types of external forces; surface forces and body forces. Surface forces, also called contact forces, arise from mechanical contact with other bodies and include friction, tensile forces, normal forces, and shearing forces. Body forces, or internal forces, are forces that act throughout the volume of a body and can be due to a force field such as gravity or electric fields, or can also be due to an outside forces influence. The magnitude of the internal forces acting on a unit cross sectional area is called the stress.[18] The intensity of the distribution, the stress σ, is just the force F divided by the unit area A,

$$\sigma = \frac{F}{A}. \tag{1.4}$$

Another key part of elastic theory is strain, ε, which is defined as the stretch or deformation of interior parts of the body per unit length,

$$\varepsilon = \frac{\Delta l}{l}. \tag{1.5}$$

Hooke's law can be written in terms of the relationship between stress and strain for perfectly elastic materials as,

$$\sigma = E\varepsilon, \tag{1.6}$$

where the constant of proportionality E is defined as the Young's modulus, or one-dimensional modulus of elasticity.

In macroscopic stress-strain experiments the strain can be measured by a strain gauge, which is fixed to the surface of the strained material and measures the elongation (or contraction) by the change in electrical resistance[18] of a coil of wire. Stress can simply be calculated, and the Young's modulus is then the slope of the stress vs. strain curve. In nanoscale experiments,

however, there exist no such strain gauges which prevent extracting the Young's modulus from a stress-strain curve's slope, requiring a different method for acquiring the Young's modulus.

One method is to call on the elementary beam theory,[3-5, 8, 9, 20] specifically the simple bending theory.[19] Consider a cantilevered beam of length L as shown in **Figure 6**. In **Figure 6** the long axis, or neutral axis, of the beam is defined to be the x direction and the point load located at x will result in a deflection in the y direction. This axis is defined as the neutral axis because for a bending moment applied in the y direction, the planes above the neutral axis are stretched while planes below the neutral axis are compressed, while the neutral axis is neither compressed nor stretched. The deflection of the beam is assumed to be constrained to the x-y plane, simplifying this to a two-dimensional problem. The other simplifying assumptions of simple beam bending theory are as follows;[19]

1. The beam is initially straight and unstressed.

2. The material of the beam is assumed to be perfectly homogenous and isotropic.

3. The elastic limit is nowhere exceeded.

4. The Young's Modulus is equivalent for bending and tension.

5. Plane cross-sections remain plane before and after bending.

6. Every cross-section of the beam is symmetric about the plane of bending.

7. There is no resultant force perpendicular to any cross-section.

A well-known formula for the deflection y of a cantilevered beam of length L subject to a point load F at x is,[19]

$$y = \frac{F(3L - x)x^2}{6EI},$$ (1.7)

where E is again the Young's modulus and I is the area moment of inertia. The moment of inertia for the silver nanorods is given by the second moment of inertia for a circular cross section of radius r,

$$I = \frac{\pi r^4}{4}. \tag{1.8}$$

Equation (1.7) allows calculation of the deflection as a function of the distance away from the fixed end of the beam. Rearranging **Equation (1.7)** by solving for the force F yields,

Substituting in **Equation (1.8)** into **Equation (1.7)** and taking the partial derivative of **Equation (1.7)**, $\frac{\partial F}{\partial y}$, yields the spring constant, k as a function of x,

$$k(x) = \frac{3\pi r^4}{2(3L-x)x^3} E \tag{1.10}$$

Since, for a cantilevered beam, the distance from the free end of the rod to the location of the point load (the force F) does not change the force constant, set L = x to yield,

$$k(x) = \frac{3\pi r^4}{4x^3} E \tag{1.11}$$

This method of finding the value of the force constant as a function of distance from the pinning point of a cantilevered beam was, to the knowledge of the author, first applied to nanorods and reported in the literature by Wong *et al.* in 1997.[8]

1.4 Glancing Angle Deposition

Glancing angle deposition (GLAD) is a type of physical vapor deposition (PVD) performed at oblique angles.[7] In a PVD experiment, the deposition source is vaporized resulting in a vapor flux that travels toward the substrate. Different evaporation methods include thermal evaporation, magnetron sputtering, electron-beam evaporation and laser ablation.[20] The vapor will undergo a phase change from vapor to solid when incident on the substrate surface. **Figure 7** shows a basic schematic of the incident vapor flux, the substrate, and the angle between them θ for glancing angle deposition.

When the direction of vapor flux and the substrate normal are parallel, uniform evaporate coverage of the substrate occurs and a thin film is fabricated. In order to create nanostructures with varying morphologies, different parameters of the deposition can be adjusted. Changing the angle of incident flux so the source and substrate normal are not parallel, or deposition at oblique angles is one possible variation that results in anisotropic sample morphology.

In oblique angle deposition, the angle measured between the vapor path and substrate normal is large, typically θ > 80°.[20] The GLAD technique makes use of the large oblique angle of incident flux to produce films with intrinsic anisotropy.[7] Anisotropy of the films is due to the atomic-scale shadowing effect from the initial nucleation sites.[7, 20] This shadowing effect occurs when the evaporant first nucleates on the surface of the substrate "shadowing" the area behind the nucleus as viewed from the deposition source from receiving further incident flux. The growth of the film from the nucleation sites is driven by adatom diffusion to energetically lower preferential sites. A schematic of this shadowing effect, adatom diffusion, including the deposition angle is found in **Figure 8.** The oblique angle technique can be modified with the addition of substrate rotation around an axis parallel to its normal.

Substrate rotation changes the net shadowing effect, causing the growth of the film to follow the apparent position of the vapor source. What results is a columnar structure that increases in length along its long axis while the incident flux is present.[7] When the substrate is patterned with periodic "plugs," the incident vapor will grow preferentially at these sites resulting in macroscopic patterning of the grown nanocolumns.[4, 20-23]

Paradigmatic examples illustrating the affect of changing deposition parameters on columnar microstructures include tilted columns, chevronic columns, chiral columns and vertical columns.[7, 20] Fixed-oblique-angle style depositions with substrate rotation result in tilted columns.[7] Chevronic columns form when the substrate is held at a fixed oblique angle and is rotated regularly in 180° intervals.[23] Chiral columns exhibiting a helical structure are what result when the substrate is slowly and continuously rotated.[7] The vertical column is the limiting case of the chiral columns. Pitch is a measure of the vertical distance gained with a complete rotation. With increasing rotational speed the pitch will decrease and ultimately approach zero which results in vertically aligned columns.[7]

These vertically aligned columns created by oblique angle deposition with varying deposition parameters exhibit differences in not only physical features, such as topology and structure, but also electrical and optical properties.[4, 7, 20-23] Of chief interest in this thesis are the mechanical properties of isolated tilted nanocolumns, in particular the modulus of elasticity or Young's modulus. Sample geometry of the tilted nanorods is well suited for the nanomechanical bending test.[5]

1.5 Chapter 1 Figures

Figure 1: Raster pattern created by the piezoelectric scanner. The y-direction is the slow scan direction and the x-direction is the fast scan direction. Image credit: Bruker Nanoscope Software (v8.10r2) Manual.
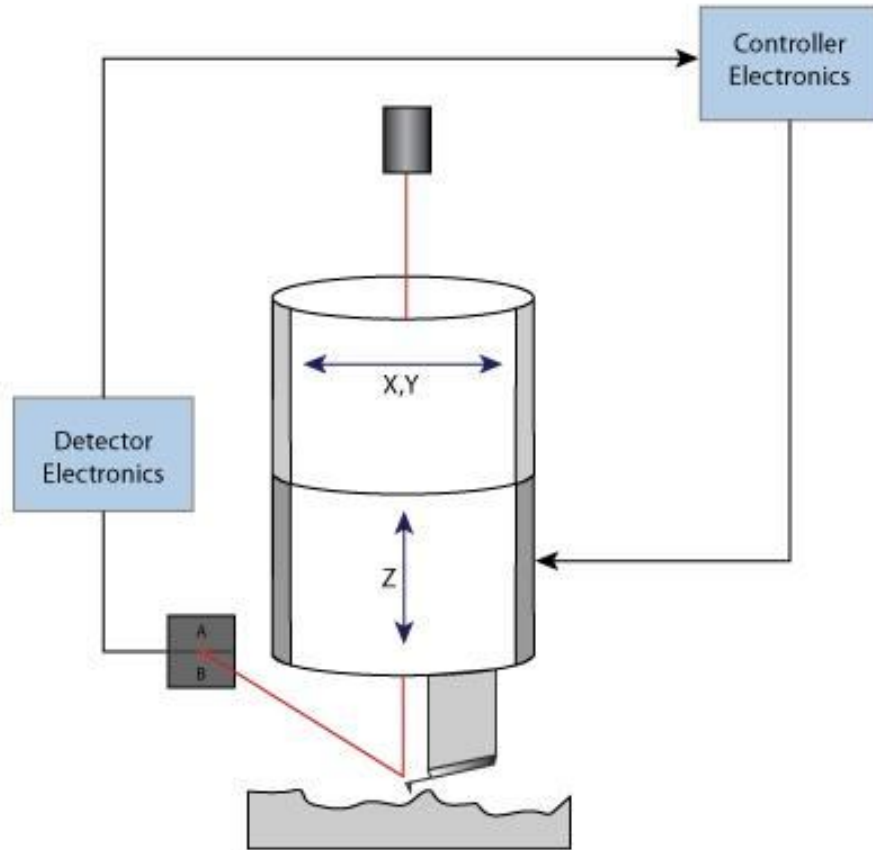
Figure 2: Basic AFM schematic showing the laser reflecting off of the back side of the cantilever, the photosensor diode, and the x-, y-, and z- directions of the piezoelectric scanner. Image Credit: Bruker Nanoscope (v8.10r12) software manual.

The Lennard–Jones 6–12 Potential
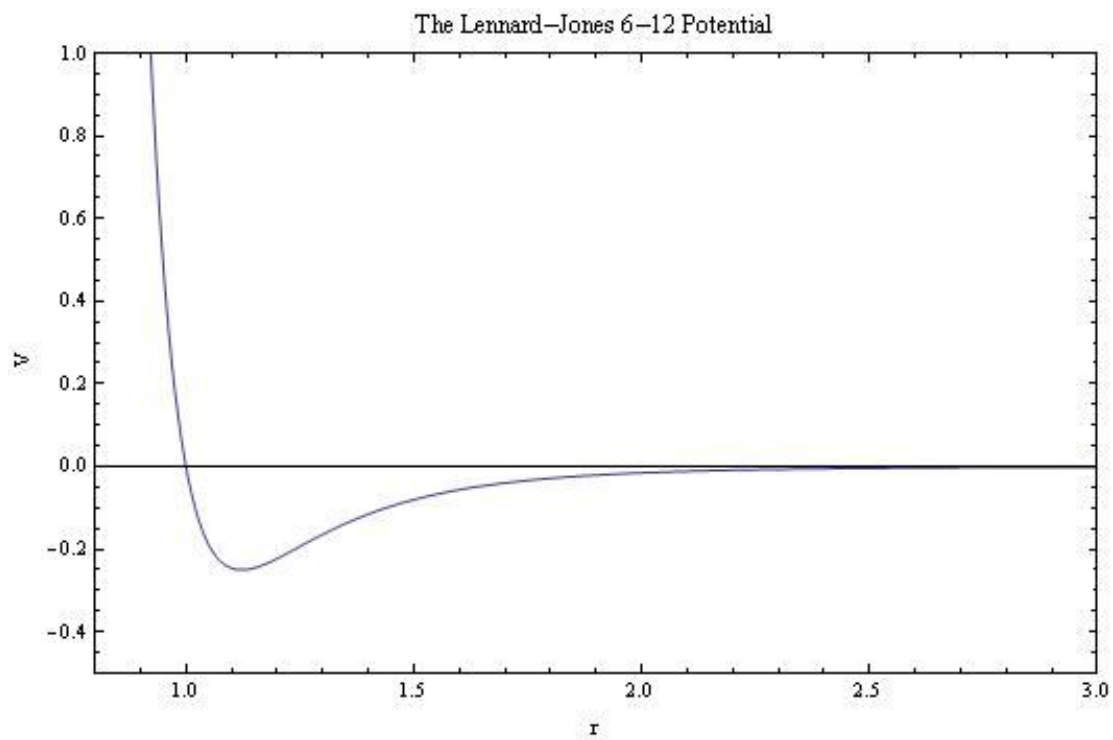
Figure 3: The Lennard-Jones potential.[24] Positive potential indicates repulsive forces and negative potential indicates an attractive force.
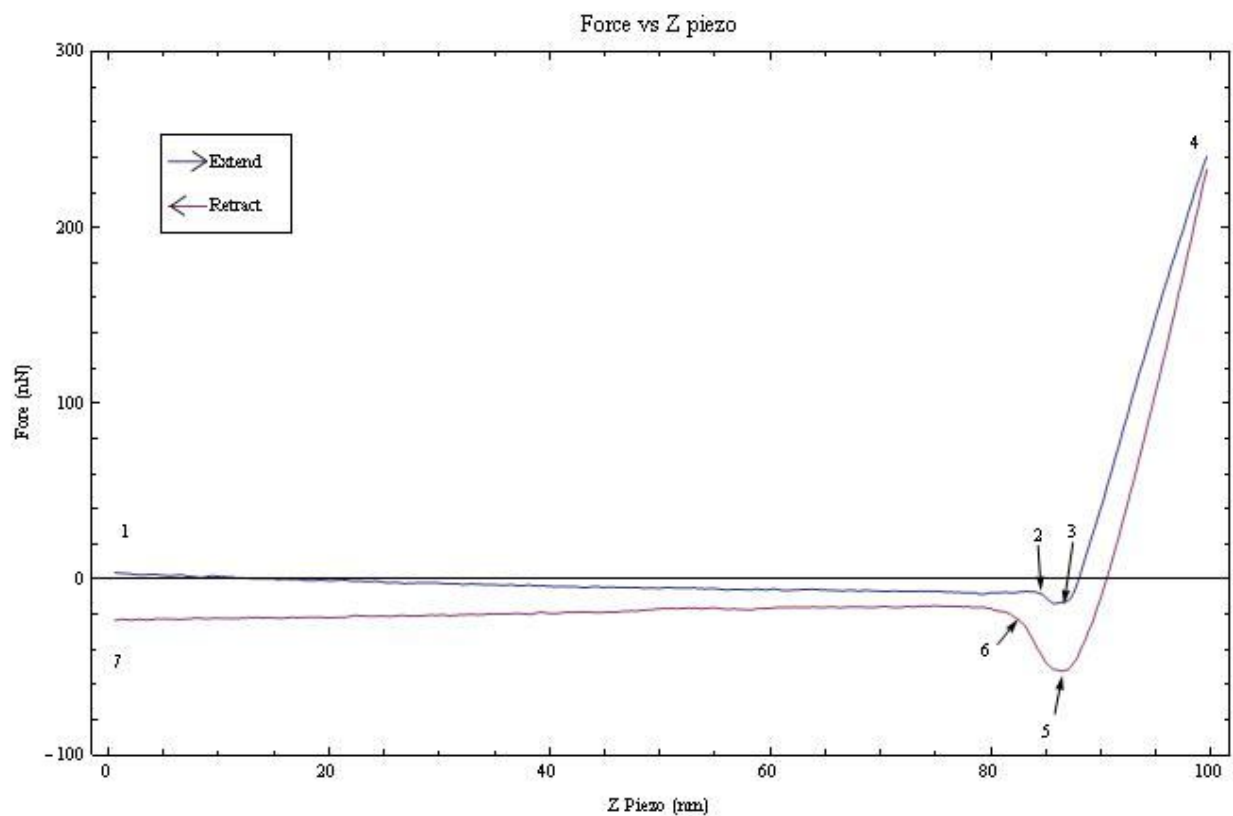
Figure 4: A force curve with z ramp size 100 nm. The z-piezo is ramped towards the surface starting at point 1 to 4 then is retracted from point 4 to 7.
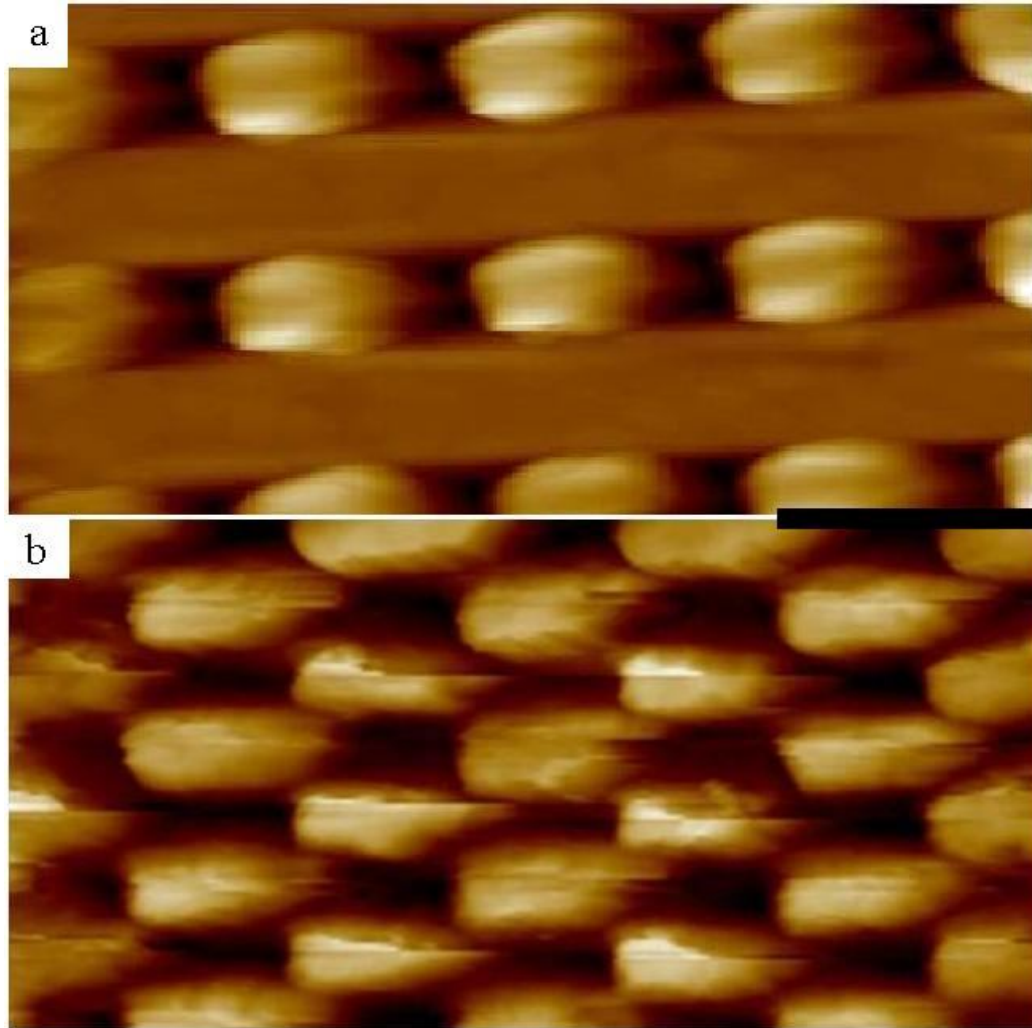
Figure 5: (a) An image taken in PeakForce QNM mode with ScanAssyst,[14] (b) An image taken in standard tapping mode exhibiting scan artifacts. The scale bar is 1μm in both images.
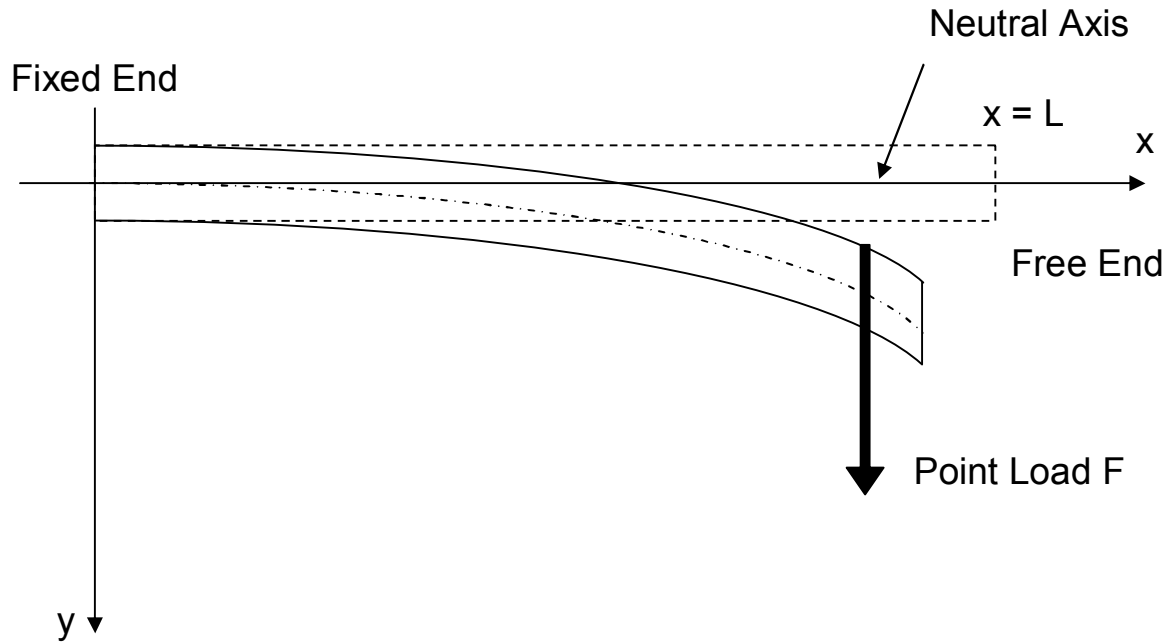
Figure 6: Cantilevered beam of length L with point load F showing the neutral axis before and after application of the point load F.
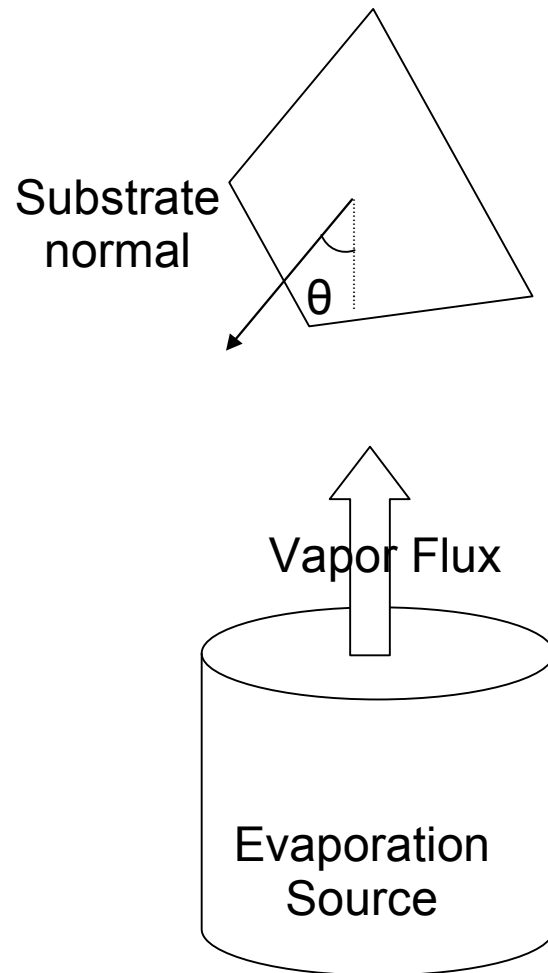
Figure 7: Schematic of a glancing angle deposition experiment, showing the evaporation source and the vapor flux travelling towards the substrate and the deposition angle θ the vapor flux makes with the substrate normal.
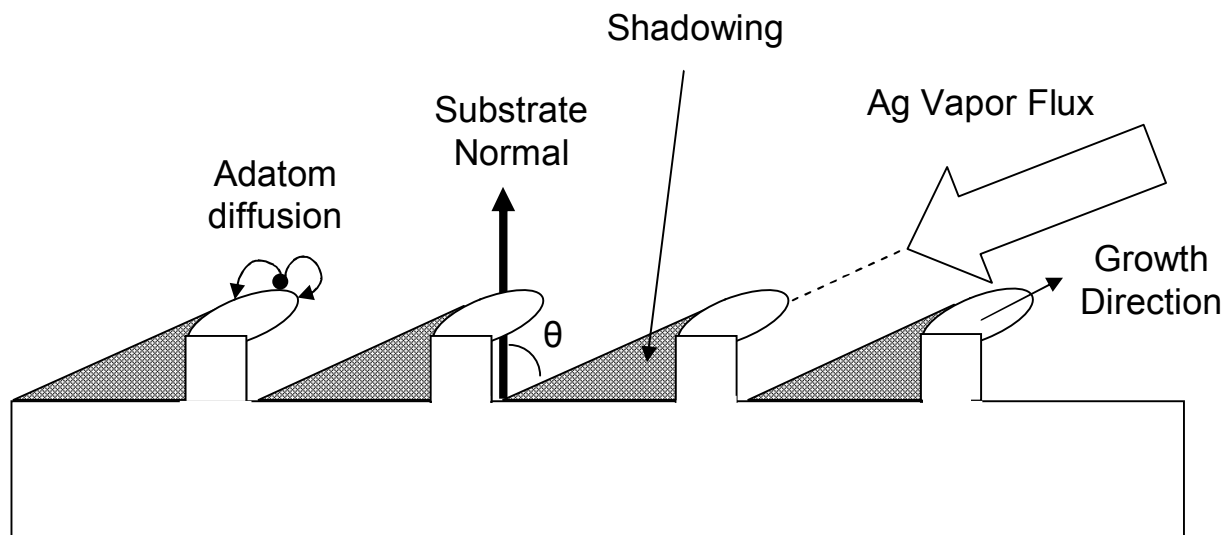
Figure 8: Diagram of mechanisms present during physical vapor deposition, showing adatom diffusion to energetically lower preferential sites, the substrate normal, the deposition angle θ, the growth direction, and the shadowing affect from the nucleation sites.

Chapter 2: Experimental Method

2.1 Sample Preparation and Characterization

Silver nanorods were prepared using the oblique angle technique with the deposition angle θ = 85˚. The silicon substrate was held fixed during deposition in order to create the nanocolumns. The substrate used was patterned with posts in a rectangular lattice with side length 1μm in order to create a well-patterned array of cantilevered nanorods favorable for mechanical bend testing.

The vacuum chamber used to grow the silver nanorod sample uses an electron beam to heat the evaporation source. Electron beam evaporation is performed by directing a beam of electrons to strike a sample in a crucible. The sample first turns molten and then begins to change into the vapor phase. The chamber has the capability to have more than one source to change from during the deposition by having several crucibles on a rotating stage. A turbo molecular pump was used to achieve a base pressure of about 5 x 10^{-7} Torr before the deposition was started. To create the silver nanorod sample, first 10 nm of titanium was deposited onto the silicon substrate, to aid in adhesion of the silver. Then the silver crucible was selected as the deposition target. The filament current was raised such that the silver deposition rate was 5 Å/s and held constant for ~30 minutes to reach a deposited film thickness of 850 nm.

A Hitachi SU-70 scanning electron microscope was used to image the sample. The accelerating voltage was set to 5 kV and the working distance was 5mm. **Figure 9** and **Figure 10** show top-down views of the nanorods. **Figure 11** and **Figure 12** show cross-sectional views. 15 nanorods were measured for their length and width using the software package ImageJ. The

average length was found to be 670 ± 10 nm, and the average width 340 ± 10 nm, which gives a radius of 170 ± 10 nm.

2.2 Nanomechanical Bending Test

As stated earlier, the patterned silver nanorod samples grown are well-suited for the nanomechanical bending test in order to measure the intrinsic spring constant and ultimately the Young's Modulus. When the AFM cantilever is in contact with a nanorod, the system can be modeled as two springs in series, and for small deformations in the elastic regime of both springs Hooke's law can be applied. The well-known formula from Hooke's law that gives the equivalent spring constant for two springs in series is,

$$\frac{1}{k_{eq}} = \frac{1}{k_{ct}} + \frac{1}{k_{nr}},$$
(1.12)

where k_{eq} is the equivalent spring constant, k_{ct} the AFM cantilever spring constant, and k_{nr} the nanorod spring constant. A schematic of the bending test is shown in **Figure 13**, while the Hookean spring system is represented in **Figure 14**. The spring constant of the nanorod can be extracted from the slope of the force versus distance curve for the nanorod-cantilever spring system. The deflection of the nanorod for the given force exerted by the cantilever can be calculated by subtracting the deflection of the cantilever from the z-piezo height,

$$\delta_{nr} = z - \delta_{ct}$$
(1.13)

When performing mechanical measurements with the AFM, selection of the AFM cantilever with mechanical properties similar to the sample is paramount. In this study the cantilevers used were MikroMasch NSC15. The backsides of the cantilevers come from the manufacturer coated with 10 nm of aluminum to increase reflectivity and therefore the sensitivity

of the optical lever scheme discussed in Section 1.2. The nominal properties of the NSC 15 Al-BS cantilevers is summarized in **Table 1**, while a schematic showing nominal dimensions is found in **Figure 15**.

The first step in the calibration procedure is to load the AFM cantilever. The laser is then aligned to the end of the cantilever, and the reflection centered on the four-quadrant PSD, with the horizontal and vertical signal reading 0 ± 0.01 V. When the cantilever is deflected, the output signal of the PSD is in volts. A sensitivity factor to convert the deflection of the cantilever from volts to the dimensionally appropriate units of nanometers is required. This parameter is called the deflection sensitivity. In order to get an accurate deflection sensitivity and to ensure a linear relationship between the z-piezo travel and the deflection of the cantilever, a sapphire (Al_2O_3) sample is loaded. Sapphire has a Young's Modulus of 345 GPa which is larger than the Young's Modulus of silicon, ensuring no deformation from the AFM cantilever. Using a rearranged version of **Equation (1.11)**, making the substitution that F/y = k the force constant and solving for E yields,

$$E = \frac{4kx^3}{wt^3} \qquad (1.14)$$

where k is the spring constant calculated from the Sader method, x is the length of the cantilever, w the width, and t the thickness. The Young's Modulus of the cantilever was calculated to be 69.0 GPa, which ensures that the monocrystalline silicon cantilever will not deform the Al_2O_3 sample. An optical microscope image used in measuring the dimensions of the cantilever is located in **Figure 16**, while the measured dimensions using the free open source software package ImageJ are found in **Table 2**.

The cantilever is ramped towards the sample, and the resulting force curve's slope in the contact regime is measured. The inverse of this slope is the deflection sensitivity. A table with

ten deflection sensitivity measurements for the cantilever used is given in **Table 3,** demonstrating the high repeatability of the deflection measurements. Plastic deformation of the AFM cantilever can result in a nonzero voltage signal from the PSD, which will invalidate furthering the experiment with a nonzero initial deflection. Realignment of the laser at this stage will also invalidate the deflection sensitivity measurement, so once the deflection sensitivity measurement is made and the PSD signal is checked to ensure a zero deflection signal, no experimental parameters can be changed without invalidating the calibration and necessitating a repeat calibration. A sample force curve from which the deflection sensitivity was measured is given in **Figure 17**. Note the lack of hysteresis in the curve demonstrating no sample deformation and linear deflection response indicating the ramp was in the elastic regime.

The Sader method[25] is the chosen method used to calculate the AFM cantilever spring constant in this study. This method is widely accepted as giving less than 15% uncertainty [26] with some reported uncertainties as low as 5%[27] and does not require destruction or modification of the cantilever, making the method both widely accessible and reliable. Sader *et al.*[25] give the equation to calculate the spring constant k as,

$$k = 0.1906\rho_f b^2 L Q \Gamma_i(\omega_f)\omega_f^2, \tag{1.15}$$

where ρ_f the density of air, ω_f the fundamental resonant frequency, Γ_i is the hydrodynamic function, b is the cantilever width, L is the cantilever length and Q the quality factor of the fundamental resonance peak.

The density of air, ρ_f is 1.2041 kg/m,[3] as given by the International Standard Atmosphere for a temperature 20˚C and pressure 101.325 kPa. Sader *et al.* recommend measurement of Q and ω_f from the power spectrum of thermal vibration in order to reduce error.[25] The power spectrum

is the fast-Fourier transform of cantilever deflection data collected over 16.5 seconds, and shows the mean squared amplitude (loosely termed power) versus frequency. A Mathematica[24] notebook was then created for fitting the power spectrum to a Lorentzian shape of the form,

$$A_w + \frac{B_0 \omega_r^4}{(\omega^2 - \omega_r^2)^2 + \frac{\omega^2 \omega_r^2}{Q^2}} , \tag{1.16}$$

where A_w is the baseline thermal noise, B_0 a Lorentzian fit parameter and ω_r is the fundamental resonance frequency. The code used to extract the parameters in **Equation (1.16)** is found in Appendix A. A power spectrum from which the Mathematica[24] notebook fits Q and ω_f is shown in **Figure 18.** The AFM software also can "auto-tune" the AFM cantilever through a range of frequencies by mechanical excitation to obtain the fundamental resonance frequency. The resonant frequency calculated by fitting the power spectrum data to **Equation (1.16)** was in agreement to the software-measured value, which was 266.6 kHz. **Table 4** shows five "tuning" measurements, and demonstrates the low uncertainty and high repeatability of the measurement of the fundamental resonant frequency.

After the above calibration is performed, the AFM is switched from contact mode to PeakForce QNM mode[14] in order to image the sample. The Bruker proprietary ScanAssyst[14] changes the scanning parameters in real-time, allowing for a virtually artifact-free topological image of the sample to be aquired without input from the user, which is invaluable when imaging a nanorod sample whose mechanical response necessitates constant adjustment of scan parameters. Once the image is captured, the AFM is switched into "Point and Shoot" mode, which allows the user to select points on the sample where force curves will be taken. Operating in this mode, force curves were taken twice at each position in 10 nm increments on five nanorods, as shown in **Figure 19**. The selected ramp size was 100 nm, since during preliminary

studies this small ramp size only resulted in elastic deformations for the Ag nanorods. The cantilever was ramped twice at each position to increase the yield of useable force curves.

Once the force curves are taken, the nanorod deflection needs to be extracted from the force curve data in order to measure the force constant k_{nr} along the length of the nanorod for fitting to **Equation (1.11)**. For that process, due to the shear volume of force curves involved, a Mathematica notebook was written to automate some aspects of analysis. The code to the notebook can be found in Appendix B, along with sufficient annotations to allow the reader to follow the procedure if they are familiar with Mathematica's language.

2.3 Chapter 2 Figures:
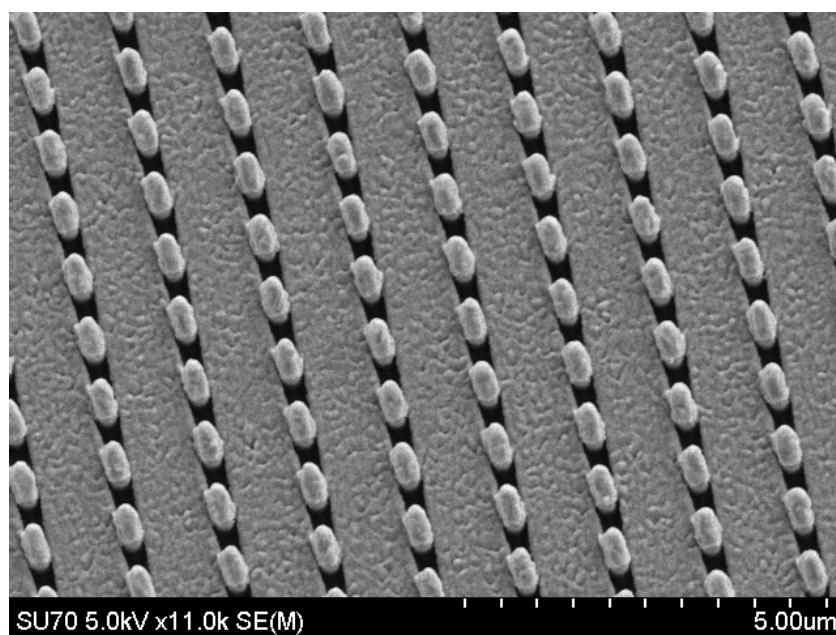
Figure 9: Top down view of the silver nanorod sample, scale is 5µm.
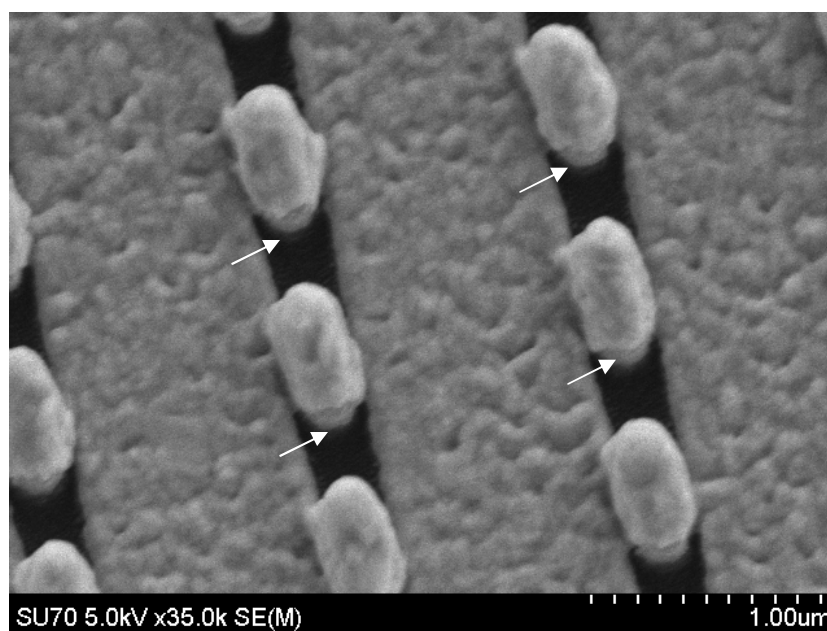
Figure 10: Top down view of the silver nanorod sample, scale is 1 µm. The post pattern is highlighted by the arrow on four nanorods, with the Ag growing on top of the post.
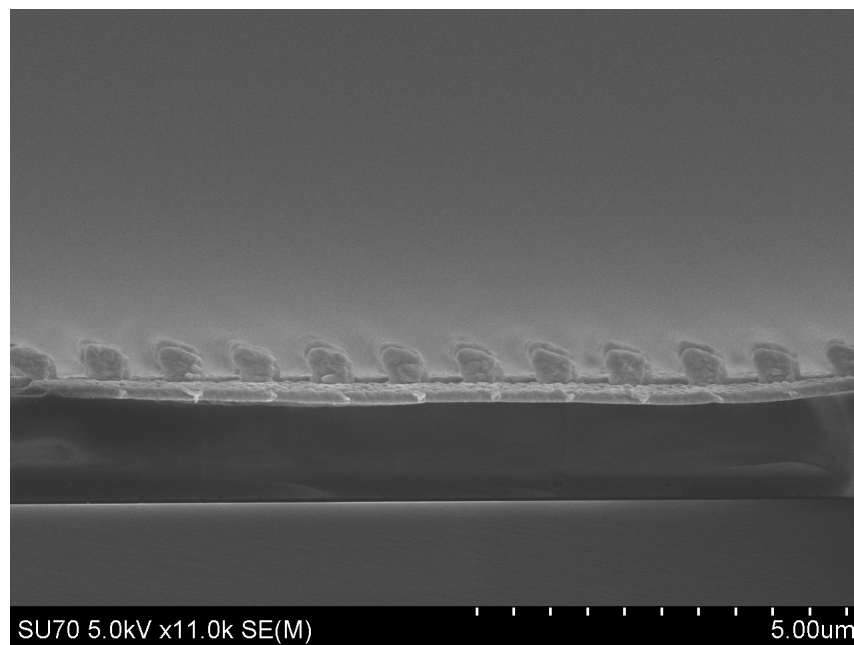
Figure 11: Cross sectional view of the silver nanorods, scale is 5 µm.
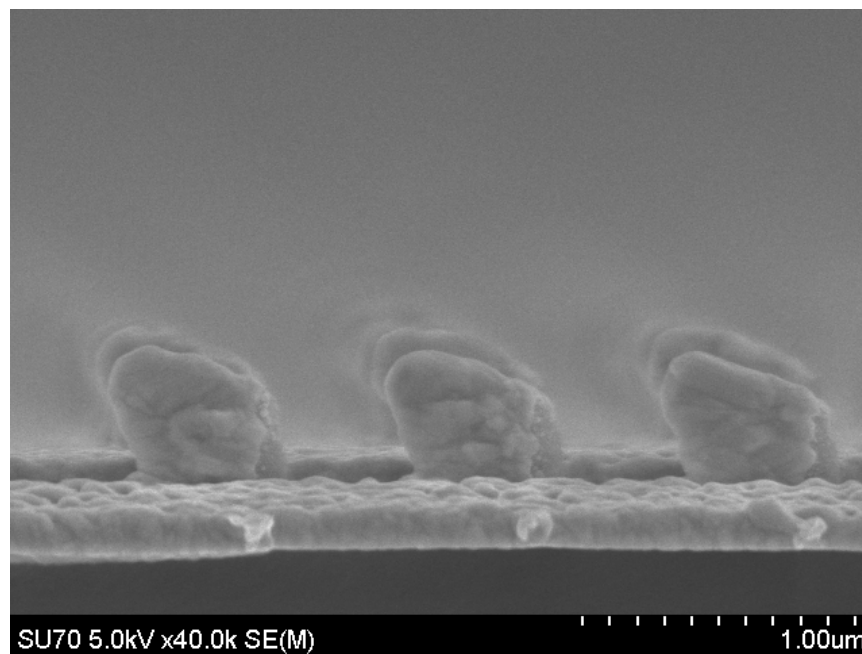
Figure 12: Cross sectional view of the silver nanorods, scale is 1 µm.
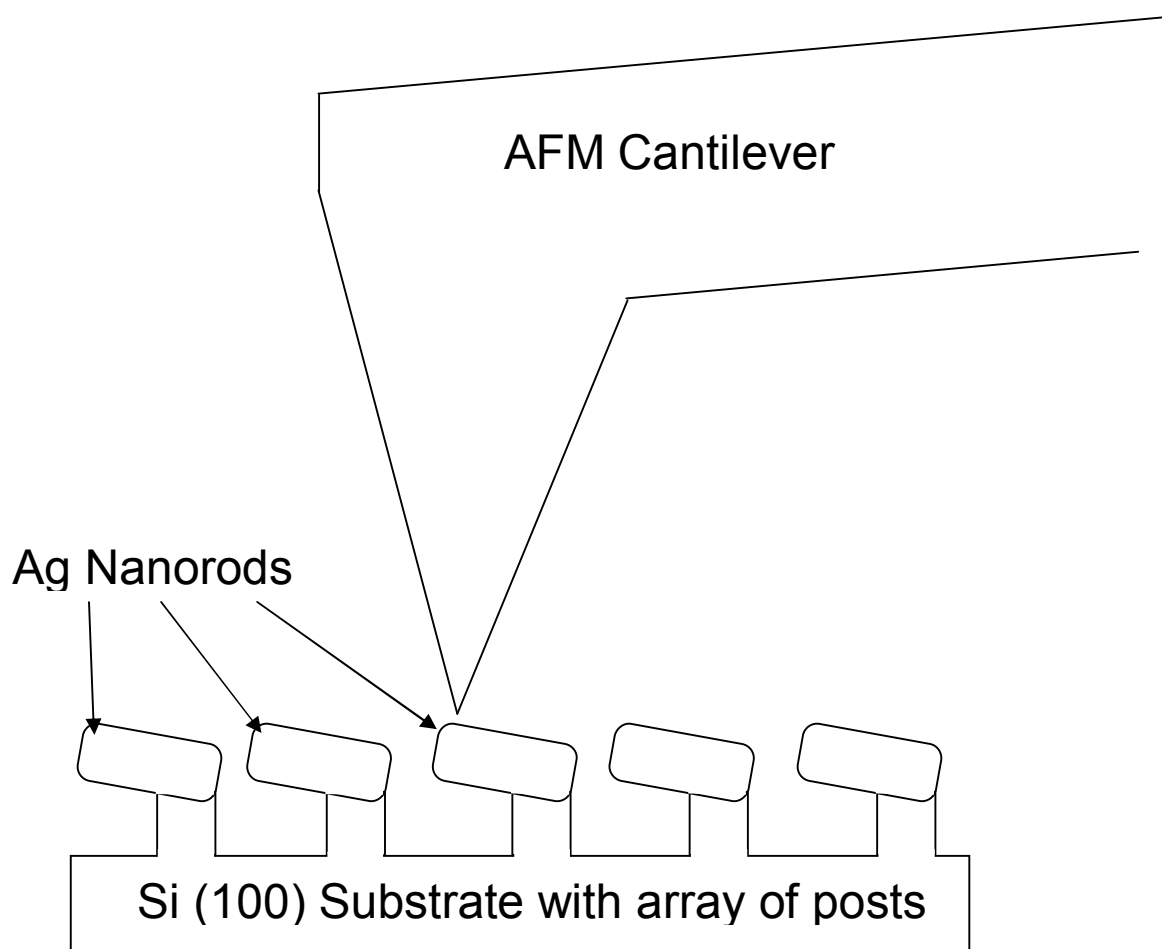
Figure 13: The bending test, showing the Ag nanorods grown on the posts on the Si substrate and the AFM cantilever.
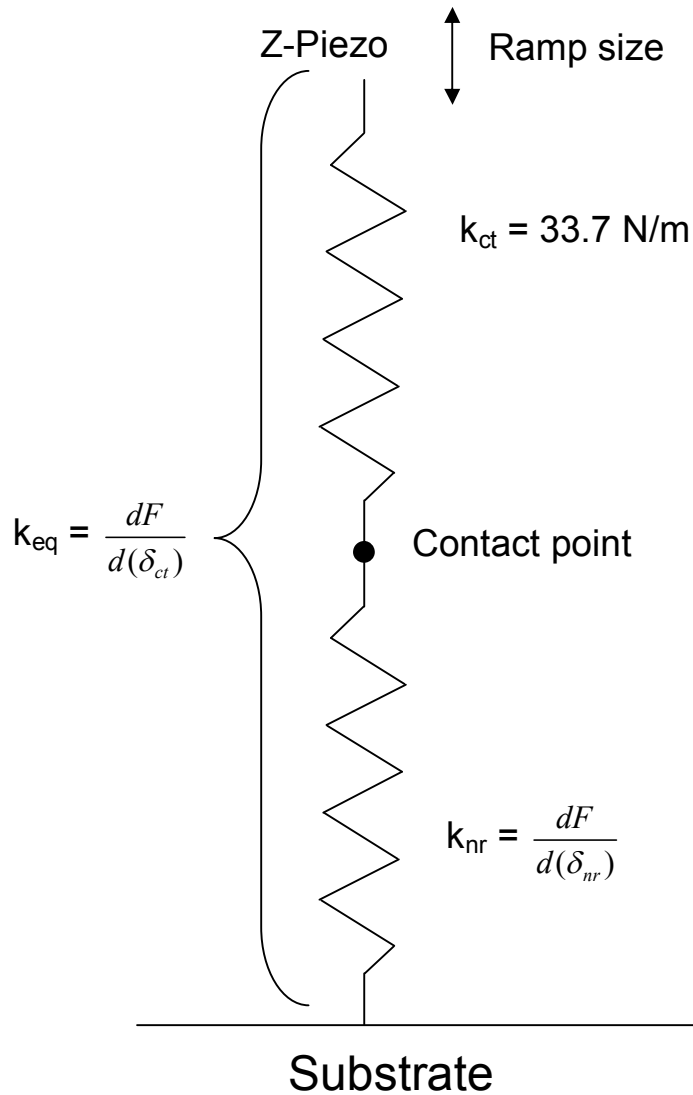
Figure 14: Schematic view of the two Hookean springs in series, the nanorod and AFM cantilever. The substrate is fixed, and the z-piezo ramps in-line with both springs. The spring constant of the cantilever k_{ct} is calculated by the Sader Method. The spring constant of the equivalent spring system is calculated from the slope of the force-distance curve in the contact regime. The slope of the nanorod k_{nr} is then calculated by plotting the force exerted by the cantilever versus the deflection of the nanorod, δ_{nr}.
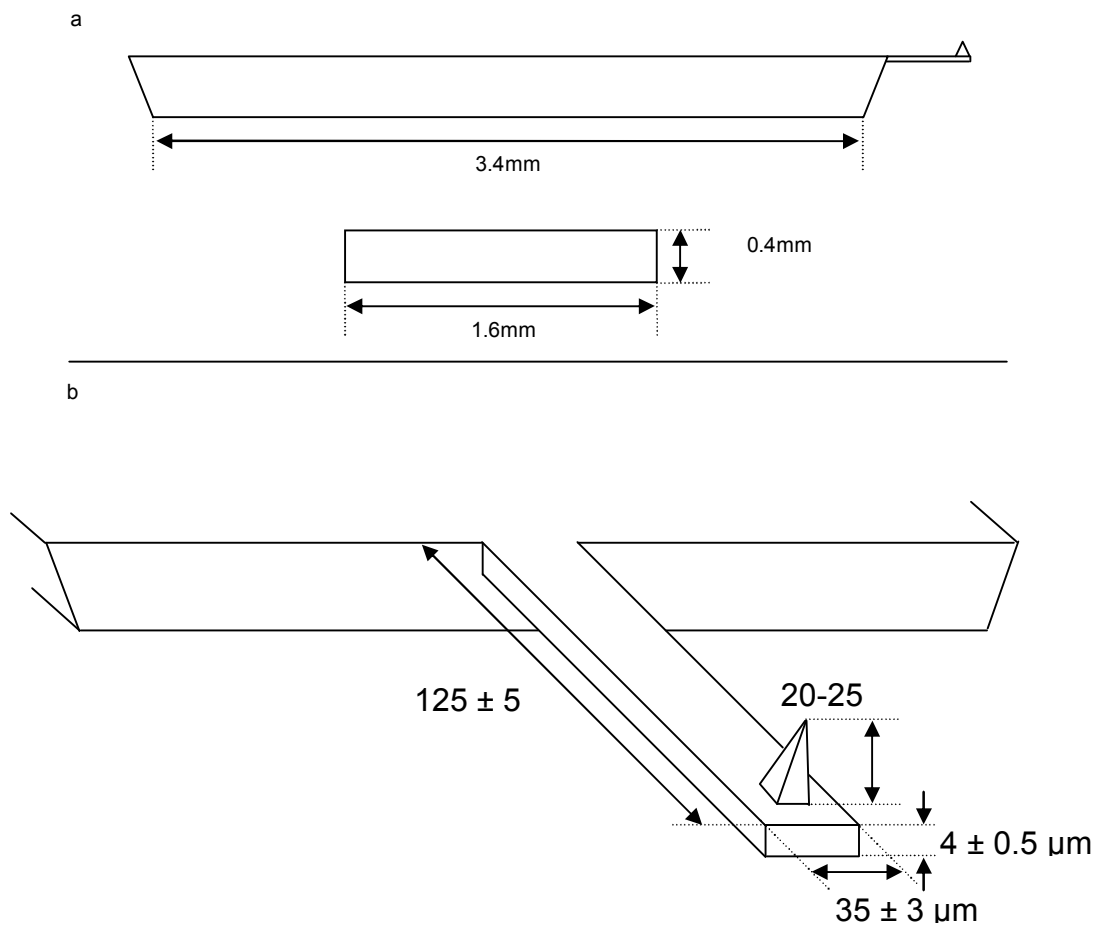
Figure 15: Schematic view of the MikroMasch NSC15 Al-BS AFM cntilever showing (a) the side view, (b) a view of the cantilever with pyramidal scanning tip.
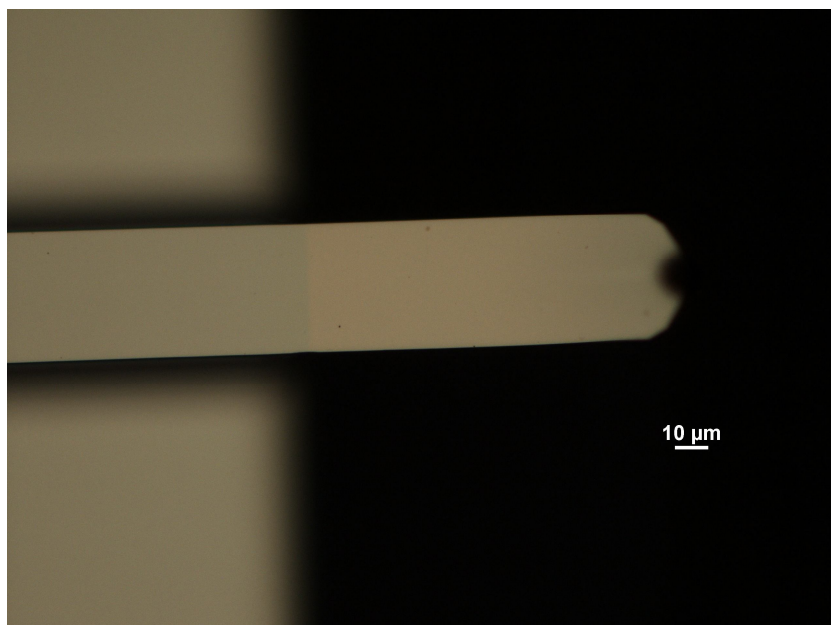
Figure 16: Optical microscope image used for measuring the dimensions of the NSC 15 cantilever found in Table 2.
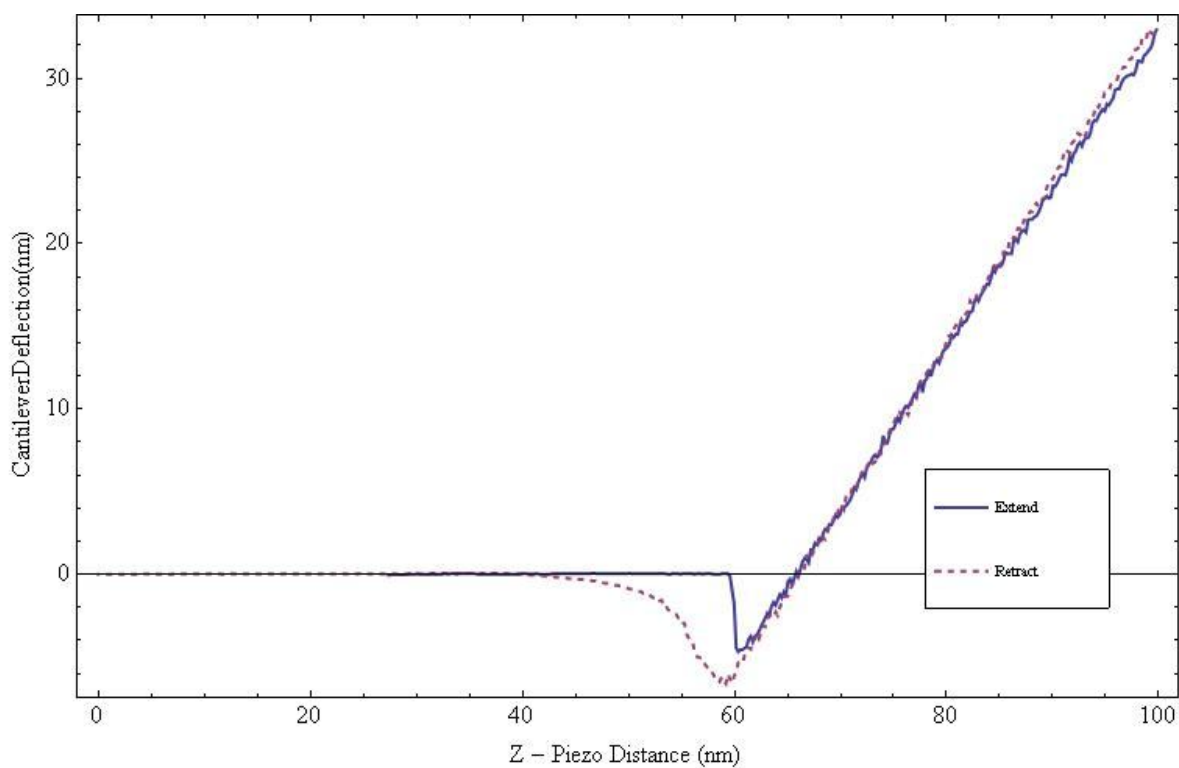
Figure 17: A sample deflection sensitivity measurement. The deflection sensitivity is the inverse of the slope. The linearity of the sloped portion indicates no sample deformation.
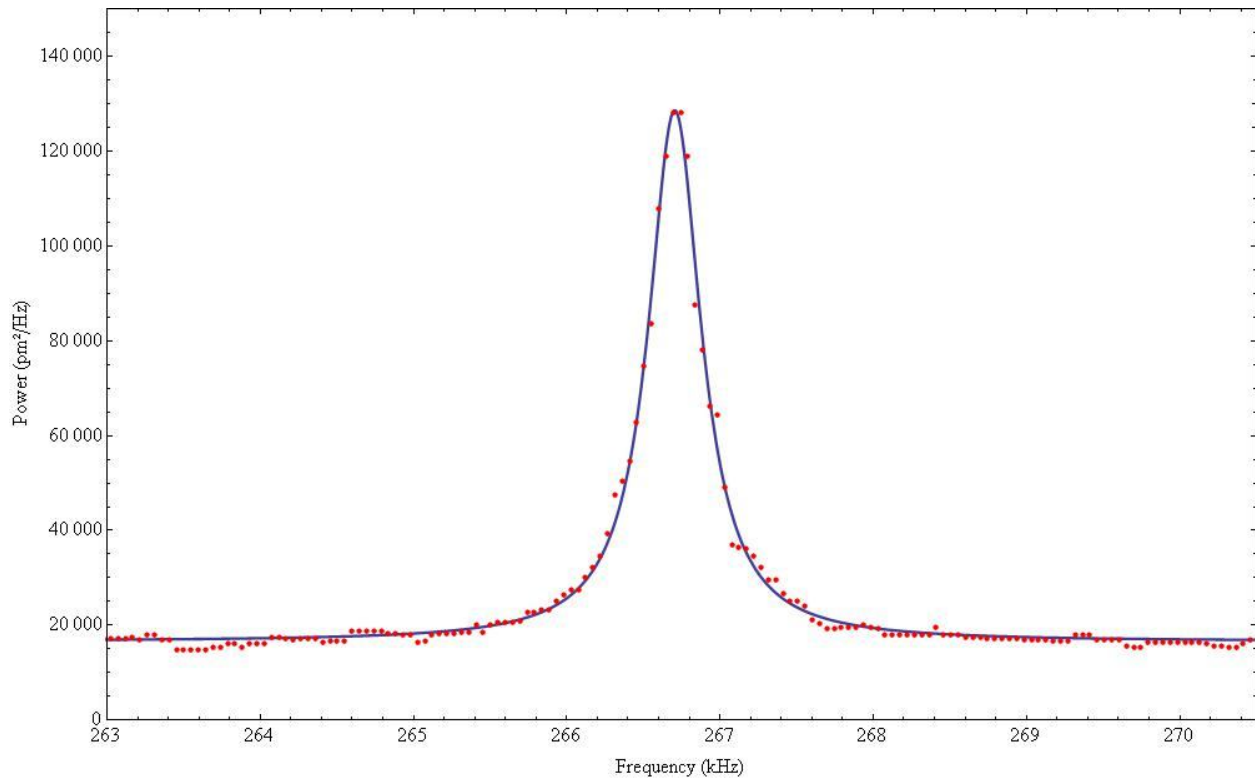
Figure 18: The power spectrum of the NSC15, showing the fundamental resonance peak at 266.6 kHz. The data are the red dots while the Lorentzian fit is the blue solid line.
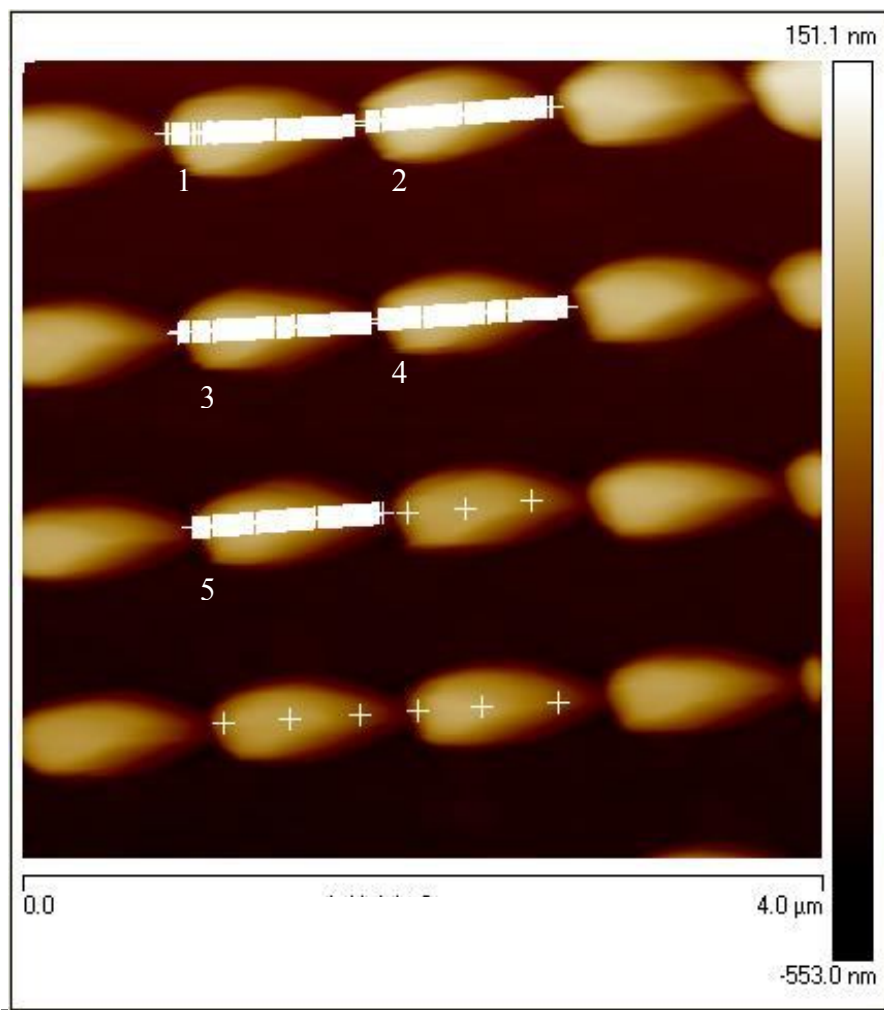
Figure 19: A screenshot taken in PeakForce QNM mode showing the 4 μm x 4 μm topographical image and the force curves, indicated by the white "+" taken in 10 nm increments along the long axis of the nanorods. The free ends of the nanorods are pointing left while the pinned ends are on the right, the measurements were made from the free end to the pinned end.

2.4 Chapter 2 Tables:

Table 1: Manufacturer quoted characteristics of the NSC 15 Al-BS.

Resonant Frequency ω_f (kHz)			Spring Constant k (N/m)			Length	Width	Thickness
min	nominal	max	min	nominal	max	(l ± 5 μm)	(w ± 3 μm)	(t ± 0.5 μm)
265	325	400	20	40	75	125	35	4.0

Table 2: Measured values of the characteristics found in **Table 1**.

ω_f (kHz)	k (N/m)	l (μm)	w (μm)
266.6	33.7	124	37.3

Table 3: Ten Deflection Sensitivity Measurements with the average and statistical uncertainty are presented.

Trial	Deflection sensitivity (nm/V)	Average (nm/V)	σ (nm/V)
1	65.87	65.97	0.16
2	65.88		
3	66.07		
4	65.99		
5	66.08		
6	65.73		
7	65.85		
8	65.95		
9	65.99		
10	66.33		

Table 4: Five measurements of the resonant frequency of the NSC 15 cantilever are presented, showing the high repeatability of the measured value for the resonant frequency of the cantilever.

Trial	ω_f (kHz)	ω_f (kHz)	σ
1	266.631	266.630	0.001
2		266.626	
3		266.630	
4		266.630	
5		266.630	

Chapter 3: Results

3.1 Results

Fitting the exported data to the model, the spring constant as a function of distance, was unsuccessful; the data exhibited no x^{-3} dependence. The data, in fact, show an increase in spring constant with an increase in distance from the pinning point of the nanorod. This is counter-intuitive, and not physically realistic. **Figures 20-29** show the first and second spring constant measurement for rods 1-5. The distance is, as stated, the distance away from the pinning point. The cantilever deflection vs. z-piezo height force curves were "filtered" using the Nanoscope software.[14] The filtering process involved visually scanning through the ~1000 force curves, and looking for "well behaved" curves, which are curves that follow the basic shape of **Figure 4** for both the extend and retract cycle. From these force curves the equivalent spring constant was calculated.

To understand this unexpected behavior, refer to **Figure 30** which shows a composite SEM image showing both the NSC15 cantilever used during this study and the silver nanorod sample. The image is to scale, so the relative sizes are exactly as they physically are. It is clear that the scattering behavior is from the cantilever interacting with more than one nanorod. In **Figure 30**, the measurements presented confirm that as the AFM tip approached the fixed end of the nanorod, due to the size of the pyramidal tip there was physical contact between the tip and the next-nearest nanorod neighbor.

In order to attempt fitting to the model, the data were also filtered after initial analysis. **Figure 31(a)** shows a well-behaved cantilever force vs. z-piezo height curve, from which the equivalent spring constant k_{eq} was calculated. **Figure 31(b)** shows a well-behaved cantilever

deflection vs. nanorod deflection plot, from the slope of which the nanorod spring constant was extracted after multiplying all of the y values by the spring constant of the cantilever to make the y-axis the force exerted by the cantilever on the nanorod. All of these types of curves were visually checked for; linearity in both the extend and retract cycles with well-behaved slopes that exhibit no singularities, that the extend and retract cycles were not too different from each other in terms of their slope, that the extend slope was less than the retract slope, and that the origin was where the curves started from. A curve that was selected as "bad" can be seen in **Figure 32.**

3.2 Chapter 3 Figures
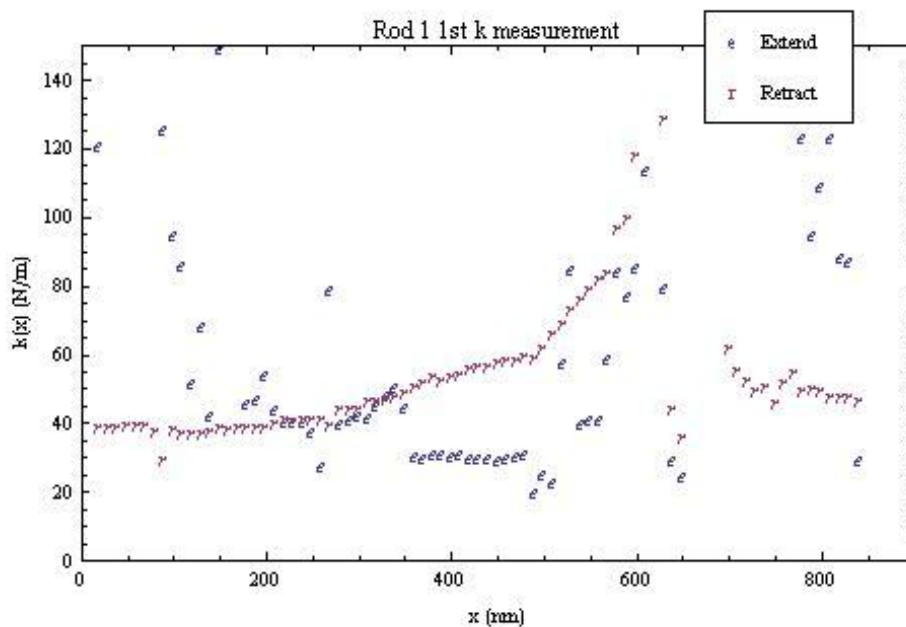
Figure 20: Rod 1 plot of the first spring constant measurement as a function of distance (k(x)). This plot is considered "well behaved" in the retract cycle before ~600 nm, while the extend cycle exhibits scatter.
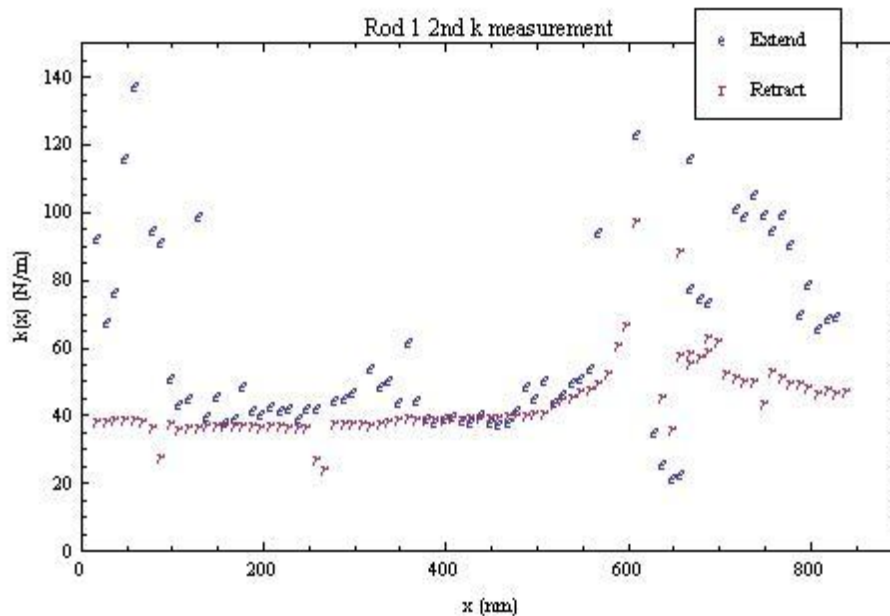
Figure 21: Rod 1 plot of the second k(x) measurement. This plot is considered "well behaved" in the retract and extend cycles before ~600 nm.
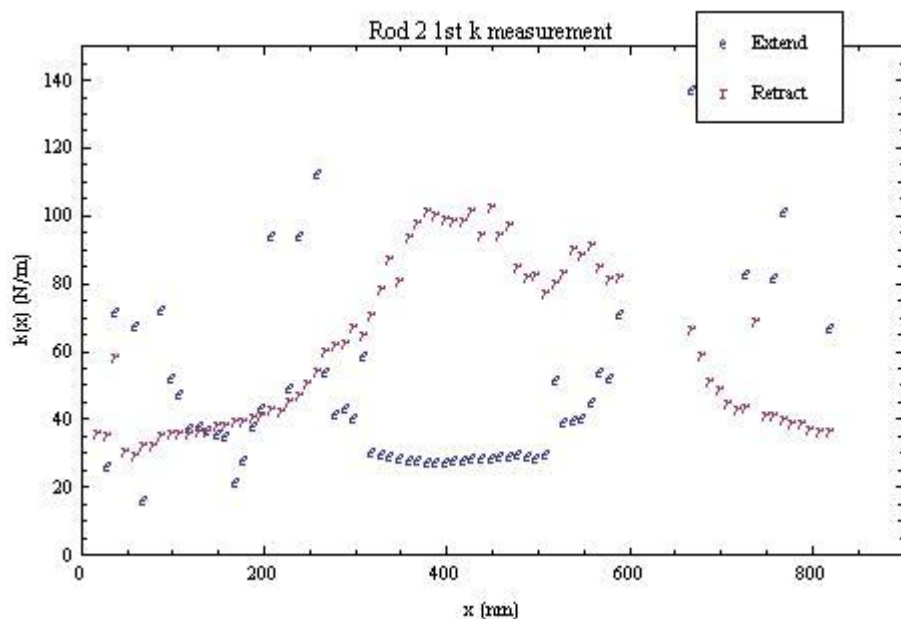
Figure 22: Rod 2 plot of the first k(x) measurement. This plot is considered well behaved in the extend cycle from ~250 until ~600 nm, while the retract cycle does not show much scatter, but does not follow expected behavior.
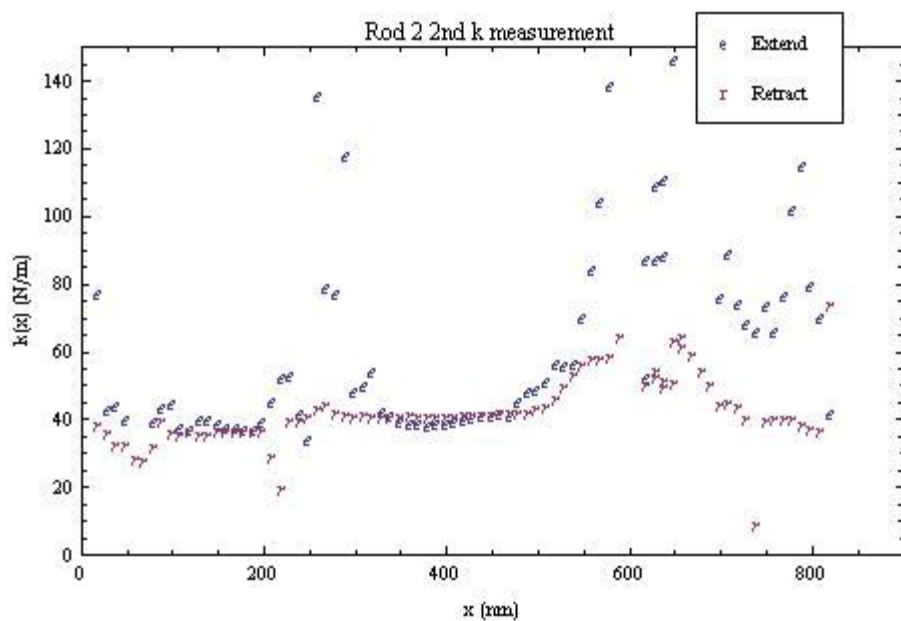
Figure 23: Rod 2 plot of the second k(x) measurement. In this plot, the extend and retract curves are in agreement until, again, about 600 nm.
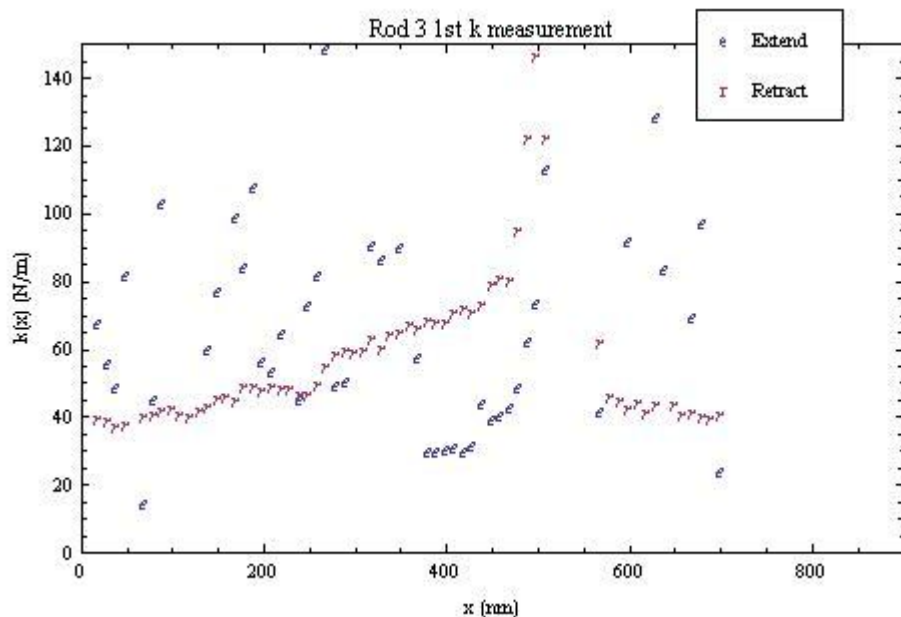
Figure 24: Rod 3 first measurement of k(x), exhibiting large scatter in both the extend and retract cycles.
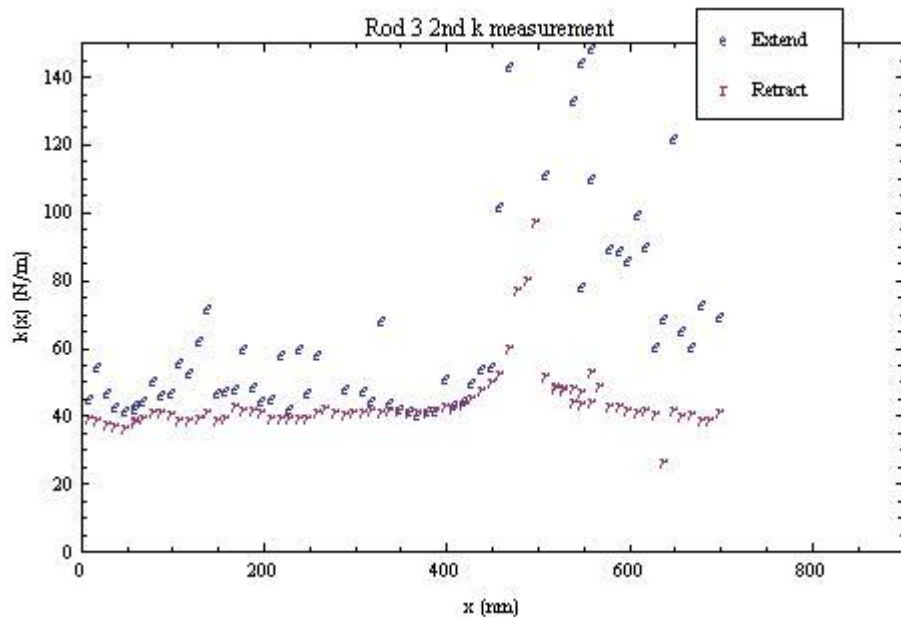
Figure 25: Rod 3 second measurement of k(x) showing good agreement between the extend and retract cycles until about 500 nm.
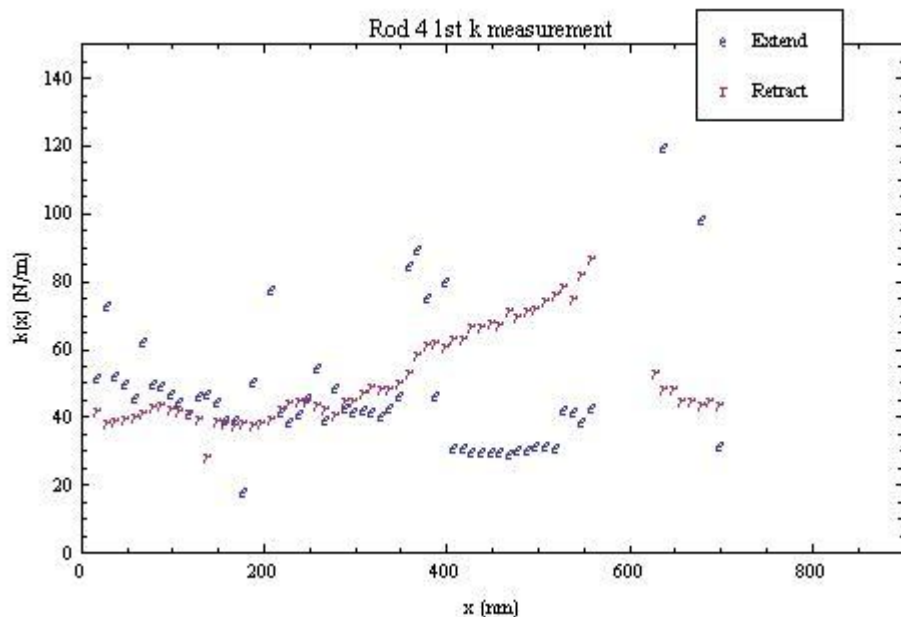
Figure 26: Rod 4 first k(x) measurement, the retract cycle is well-behaved before 600 nm, while the extend curve exhibits scatter.
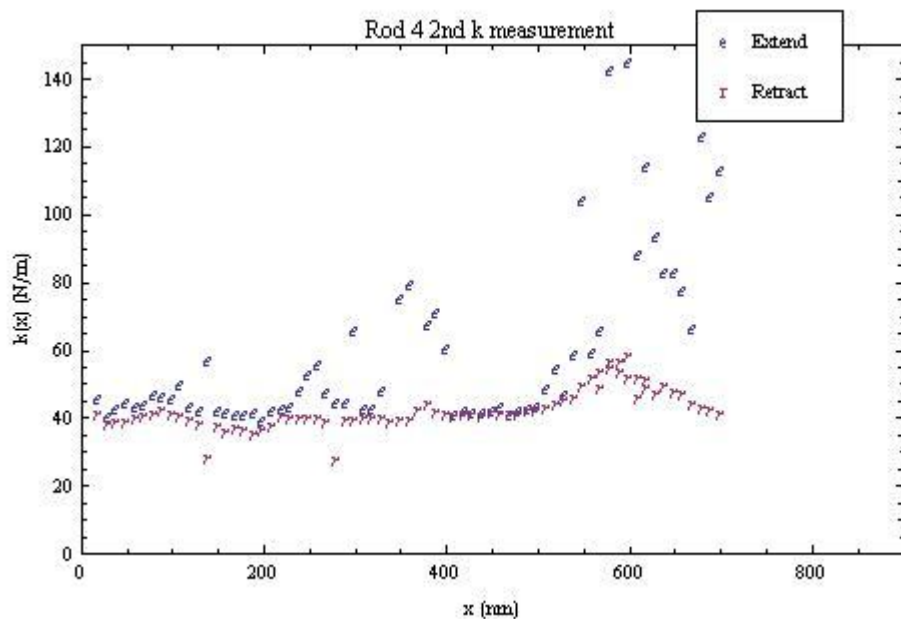
Figure 27: Rod 4 second k(x) measurement, showing good agreement between the extend and retract cycles until about 600 nm.
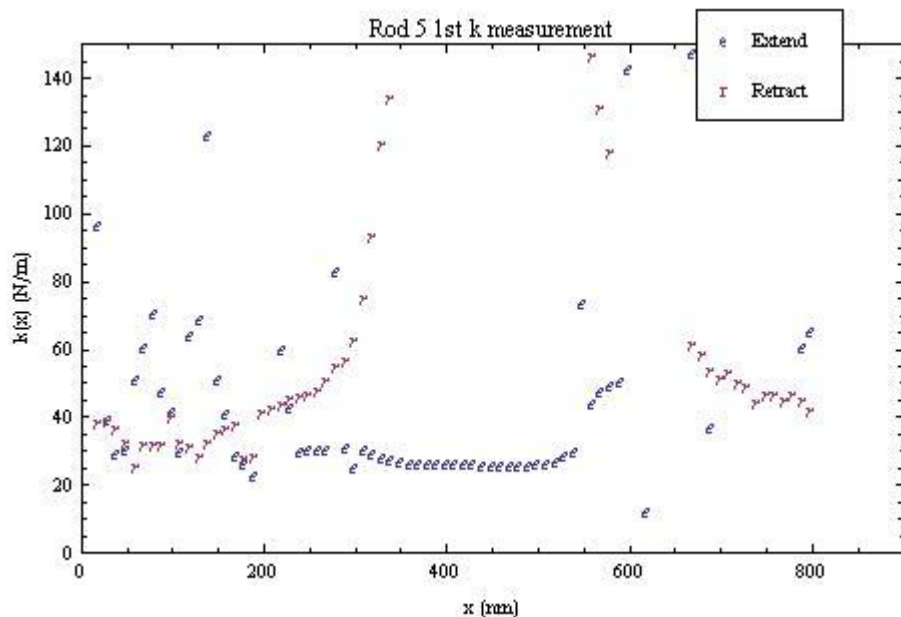
Figure 28: Rod 5 first k(x) measurement, showing large scatter in the retract cycle but is well behaved in the extend until about 600 nm.
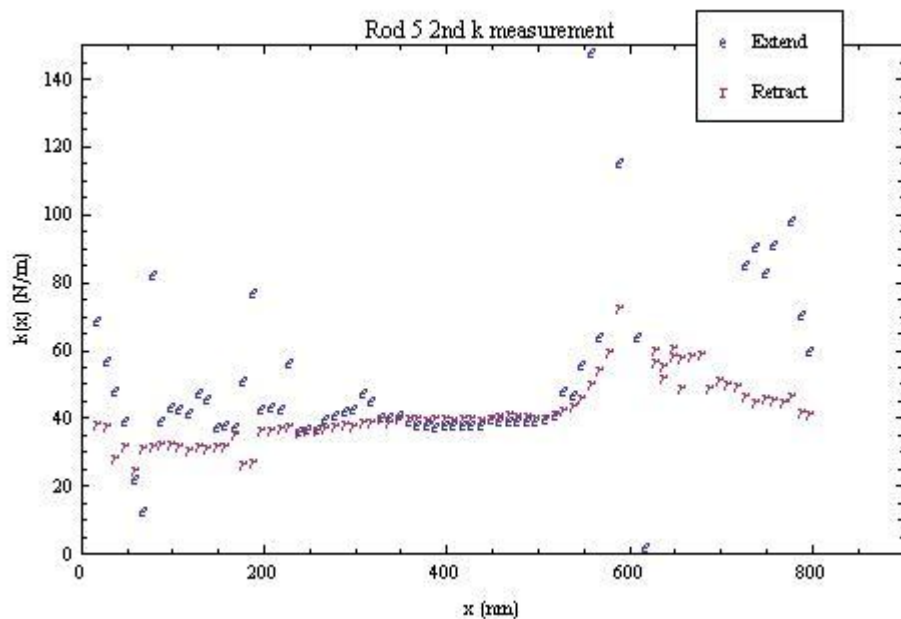
Figure 29: Rod 5 second k(x) measurement, showing good agreement between the extend and retract cycles until about 600 nm.

AFM cantilever scan direction

1 – 450 ± 10 nm
2 – 400 ± 10 nm
3 – 400 ± 10 nm
4 – 150 ± 10 nm

SU70 5.0kV x40.0k SE(M)   1.00um
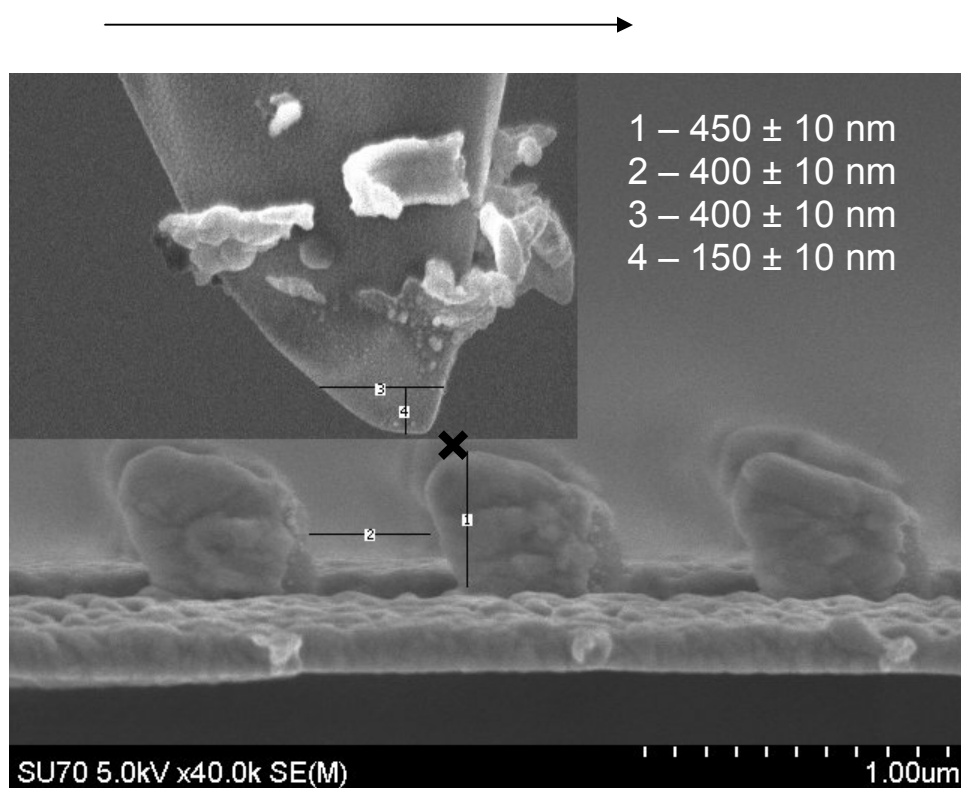
Figure 30: SEM composite image of the NSC15 used during mechanical testing and the Ag nanorod sample, both images have the same scale. The "X" marks the approximate position on the free end of the nanorod assumed for where the last "well behaved" force curves were taken. The value of the spring constant used in calculating the Young's modulus was taken from this point.

a)

b)
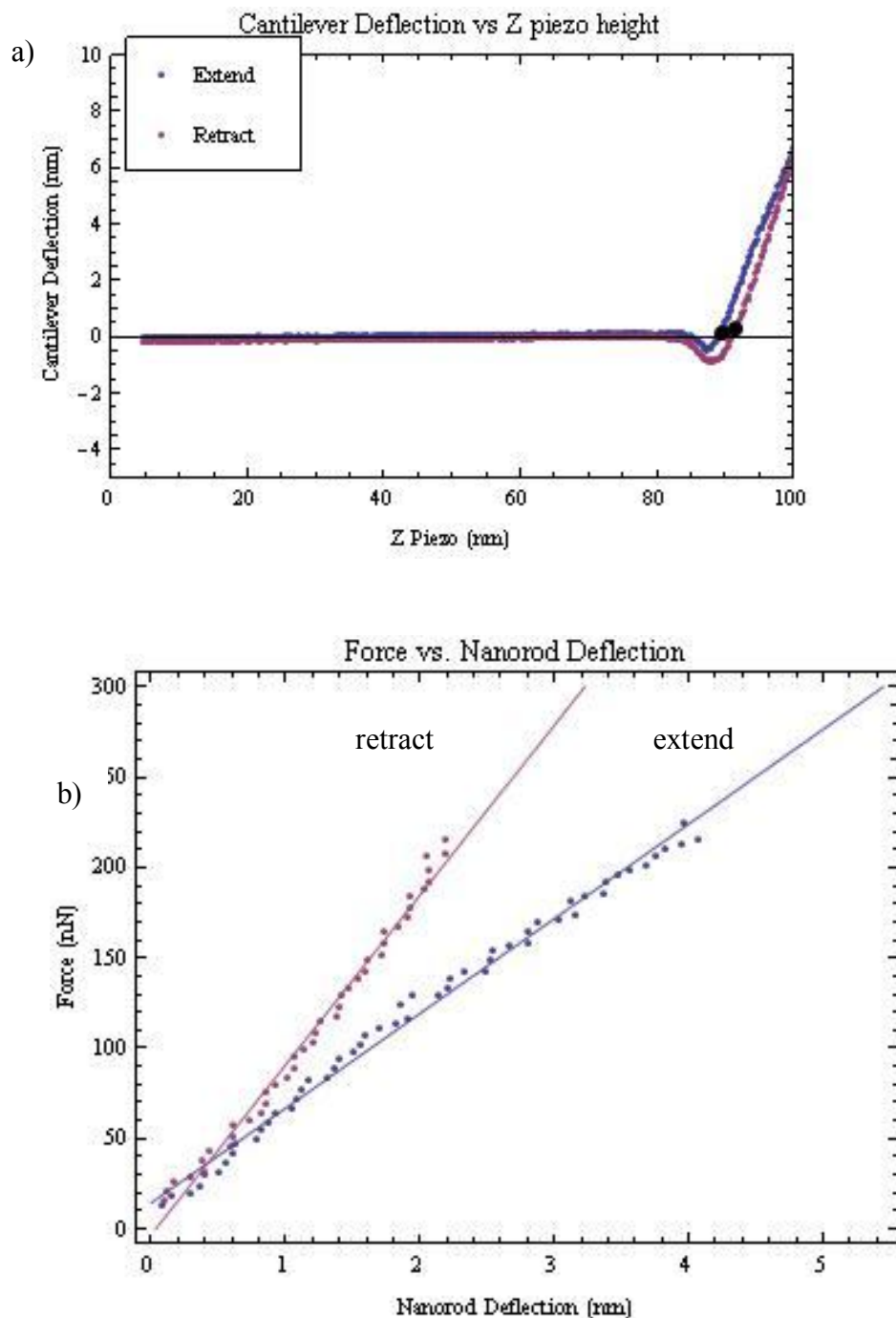
Figure 31: The blue points are the extend cycle, and the red are the retract cycle on both plots: (a) A cantilever deflection vs. z piezo height plot, from which k_{eq} was calculated. The black dots show what the Mathematica program considered as the contact point, and thus only extracted information from the contact regime to the right of these points. (b) A cantilever force vs. nanorod deflection plot, from which k_{nr} was calculated from the slope of the model fit (solid line). The retract cycle always exhibits a steeper slope due to the adhesive forces present.
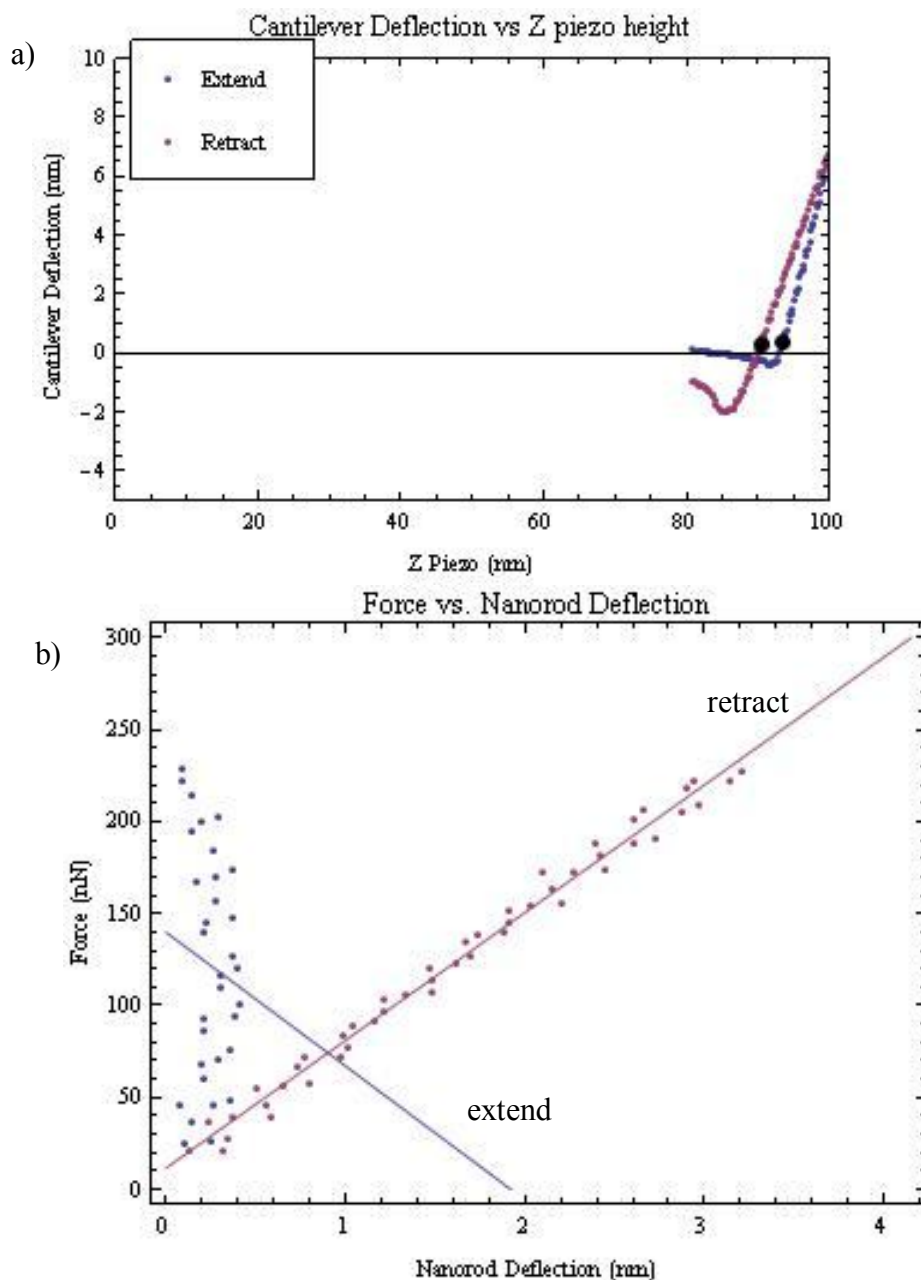
Figure 32: (a) A well-behaved cantilever deflection vs. z-piezo height force curve from which the equivalent spring constant k_{eq} was calculated. The extend cycle is blue and the retract cycle is red. Here the curves are confined to between when the piezo was between 80 – 100 nm in the ramp cycle due to the filtering process: In order to process the data with Mathematica, the two lists of points need to be the same length. The AFM software does not always record the entire ramp cycle due to nonlinearity in the z-piezo, but as long as the contact-regime is there the data are considered to be valid. (b) The filtered force vs. nanorod displacement curve. This was chosen as bad data due to the perpendicular nature of the extend cycle with regard to the retract cycle.

Chapter 4: Conclusion and Future Work

4.1 Conclusion

The data did not fit the model, and it was shown that the data did not fit possibly due to experimental difficulty. A proposed explanation for the experimental difficulty is the violation of the boundary conditions in the experiment. Specifically, the simple beam bending model requires the fixed end of the cantilevered beam to be just that, fixed on an infinitely rigid support. This condition may not exist experimentally, meaning the pinning point of the nanorod on top of the post cannot be assumed to be infinitely rigid.

Another possible source of difficulty is the geometric nature of the nanorods. The beam bending model assumes a length to width aspect ratio of greater than 10, whereas the nanorods in this study had an aspect ratio closer to 5. This means that the part of the nanorod that was actually a "cantilevered beam" was the part that was not attached to the post, and was not long enough to exhibit cantilevered beam behavior.

In conclusion, the mechanical bending test was carried out on Ag nanorods using an AFM. Large scatter and unexpected behavior was observed in the measured spring constant, which impacted the calculation of the Young's modulus. The data were not analyzed further due to the fact that the data did not fit the model, and thus the model can be assumed to be insufficient for this experiment.

4.2 Future Work

It is apparent that the experimental results from the bending test can yield not only physically unrealistic values for the Young's modulus, but also show puzzling counter-intuitive behavior. As discussed in the previous section, boundary conditions are imperative to experimental success and should not simply be assumed but verified. Verification of the nanorod pinning position would entail further SEM studies, and perhaps performing yield and fracture experiments with different adhesion layer thicknesses to investigate the affect of the adhesion layer on nanorod pinning.

One different experimental approach that may yield more reliable Young's modulus measurements may be to perform the AFM bending test inside an SEM chamber where visual confirmation can be made of the fixed end of the nanorod. Another characterization technique called X-ray diffraction can be used to investigate the strain on an inter-atomic level, which can lead to measurement of the Young's modulus [31].

Another future study that could be undertaken is to grow longer silver nanorod specimens that have a length to width aspect ratio that is greater than 10. This would not preclude using the beam bending model as the analysis procedure, and would most likely yield rods that actually exhibit the proposed behavior.

References

[1] Bhattarai S.R, Bhattarai N, Yi H.K, Hwang P.H, Cha D.I, and H.Y. Kim. "Novel biodegradable electrospun membrane: scaffold for tissue engineering." *Biomaterials* 25 (2004).

[2] Chatterjee A and B.L. Deopura. "Carbon nanotubes and nanofibre: an overview." *Fiber Polym*. 3.4 (2002)

[3] Sundararajan S, Bhushan B, Namazu T, and Y. Isono. "Mechanical property measurements of nanoscale structures using an atomic force microscope." *Ultramicroscopy* 91 (2002)

[4] Singh, J.P, Karabacak, T, Ye, D-X, Liu D-L, Picu, C, Lu T-M, and G-C Wang. "Physical properties of nanostructures grown by oblique angle deposition." *J. Vac. Sci. Technol*. B. 23.5 (2005): 2114-2121.

[5] Tan, EPS and CT Lim. "Mechanical Characterization of Nanofibers – A Review." *Composites Science and Technology* 66 (2006): 1102-1111.

[6] Haque M.A and M.T.A. Saif. "A review of MEMS-based microscale and nanoscale tensile and bending testing." *Exp. Mech*. 43.3. (2003)

[7] Hawkeye, Matthew M, and Michael J Brett. "Glancing angle deposition: Fabrication, properties and applications of micro- and nanostructured thin films."*J. Vac. Sci. Technol. A*. 25.5 (2007): 1317-1334.

[8] Wong, Eric W, Sheehan, Paul E and Charles M. Lieber. "Nanobeam Mechanics: Elasticity, Strength and Toughness of Nanorods and Nanotubes." *Science*. 277 (1997)

[9]Gaire C, Ye, D-X, Tang F, Picu R.C, Wang G.-C, and Lu T.-M. "Mechanical Testing of Isolated Amorphous Silicon Slanted Nanorods." *Journal of Nanoscience and Technology*. 5 (2005)

[10] Nagar, Rupali, Kanjilal D, Mehta B.R, and Sing J.P. "Tailoring the spring constant of Si nanorod structures using swift heavy ion irradiation." *Nuclear Instruments and Methods in Physics Research B*. 267 (2009)

[11] Binnig G, Quate CF and Ch. Gerber. "Atomic Force Microscope." *Physical Review Letters* 56.9 (1986): 930-933.

[12] Seo, Yongho and Jhe, Wonho. "Atomic Force Microscopy and Spectroscopy." *Reports on Progress in Physics*. 71 (2008)

[13] Ashcroft, Neil, and N. David Mermin. *Solid State Physics*. Belmont: Brooks/Cole, 1976. 398-400.

[14] Peakforce Quantitative Nanomechanical Mapping Package (Installed on Nanoscope Software Version 8.12r12) [Software]. (2012). Santa Barbara, Ca: Bruker AXS.

[15] R.T. Gunther. *Early Science in Oxford*, volume 8. Oxford University Press, Oxford. 1931.

[16] Cleland, Andrew N. *Foundations of Nanomechanics: From Solid-State Theory to Device Applications*. Heidelberg: Springer-Verlag Berlin, 2003. Print.

[17] "Hooke's Law." Wikipedia Foundation, Web. 7 Apr 2012. <http://en.wikipedia.org/wiki/Hooke's_law>.

[18] Timoshenko, S.P., and J.N. Goodier. *Theory of Elasticity*. 3rd Edition. McGraw-Hill, 1934.

[19] Hearn, E.J. *Mechanics of Materials*. 2nd Edition. 19. Elmsford: Pergamon Press, 1985.

[20] Ye, D.X, Karabacak, T, Picu R.C, Wang G-C, and T-M Lu. "Uniform Si nanostructures grown by oblique angle deposition with substrate swing rotation." *Nanotechnology* 16. (2005): 1717-1723.

[21] Zhao, Y-P, Ye, D-X, Wang, G-C, and T-M Lu. "Novel Nano-Column and Nano-Flower Arrays by Glancing Angle Deposition." *Nano Letters*. 2.4 (2002): 351-352.

[22] Ye, D-X, Zhao, Y-P, Yang, G-R, Zhao, Y-G, Wang, G-C and T-M Lu. "Manipulating the column tilt angles of nanocolumnar films by glancing-angle deposition." *Nanotechnology* 13 (2002): 615-618.

[23] Ye, D-X, Karabacak, T, Lim, B K, Wang, G-C and T-M Lu. "Growth of uniformly aligned nanorod arrays by oblique angle deposition with two-phase substrate rotation." *Nanotechnology* 15 (2004): 817-821.

[24] Mathematica (8.0.4.0) [Software]. (2012) Wolfram Research Inc.

[25] Sader, John, James Chon, and Paul Mulvaney. "Calibration of rectangular atomic force microscope cantilevers."*Review of Scientific Instruments*. 70.10 (1999)

[26] Kim, Min-Seok, Jae-Hyuk Choi, Jong-Ho Kim, and Yon-Kyu Park. "Accurate determination of spring constant of atomic force microscope cantilevers and comparison with other methods." *Measurement*. 43. (2010)

[27] Ohler, Ben. "Practical Advice on the Determination of Cantilever Spring Constants." *Veeco Application Note*. 2007.

[28] Manoharan M.P, Desai A.V, Neely G, and Haque M.A. "Synthesis and Elastic Characterization of Zinc Oxide Nanowires." *Journal of Nanomaterials*. (2008)

[29] Erdelyi R, Halasz V, Szabo Z, Lukacs I.E, and J. Volk. "Mechanical Characterization of epitaxially grown zinc oxide nanowires." *Physica E* (2011)

[30] Maranganti, R, Sharma N. D and P Sharma. "Electromechanical coupling in nonpiezoelectric materials due to nanoscale nonlocal size effects: Green's function solutions and embedded inclusions." *Physical Review B*. 74 (2006)

[31] Goudeau, P, Villain, P, Tamura N, Renault P.-O, Badwi K.F, and H. A. Padmore. "Elastic Properties of Supported Polycrystalline Thin Films and Multilayers: an X-ray Diffraction Study." Materials Science Forums. 426-432 (2003) 3409-3414.

Appendix A: Fitting Power Spectrum data to a Lorentzian

Import the data file

```
psd1 = Import[
    "C:\\Documents and Settings\\PHYS_grad\\My Documents\\kennysm\\Thesis\\data\\NSC15
      calibration\\nsc15 1 tune\\nsc15albssappcalib32666321 483911Nm.txt", "Data"];
fund = 266; (*Guess the fundamental resonant frequency*)
peakl = fund - (0.1 * fund);
peakr = fund + (0.1 * fund);
psd = Drop[psd1, 1];

ListPlot[psd,
 Frame → True,
 FrameLabel → {"Frequency (kHz)", "Power (pm²/Hz)"} ,
 PlotRange → {{peakl, peakr}, {0, 150000}},
 FrameStyle → Directive[16, Black],
 ImageSize → 400,
 PlotStyle → {Thickness[0.0025]}]
```
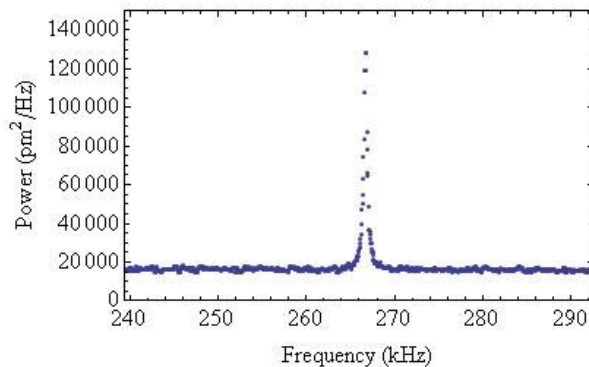

Isolate the resonance peak (red):

Use the peakbottom variable to estimate the y value of the bottom of the resonance peak.
Use peakl and peakr to estimate the x values of the sides of the peak.
Peak is an estimate of the resonant frequency, if you have chosen the peak sides correctly.
Peakmax is the maximum y value of the peak.
Be sure to update the baseline plot below also

```
peakbottom = 16000; peakl = 265; peakr = 268.5; peak = (peakl + peakr) / 2; peakmax = 150000;
spike0 = Select[psd, #[[2]] > peakbottom &];
(*Select the points greater than the peak bottom threshold set*)
spike = Select[spike0, peakl < #[[1]] < peakr &];
(*Select the points between the left and the right set values*)
ListPlot[spike,
 PlotStyle → Red,
 Frame → True,
 FrameLabel → {"Frequency (kHz)", "Power (pm²/Hz)"},
 PlotRange → {{peakl - 5, peakr + 5}, {0, peakmax + 0.5}},
 ImageSize → 400, (*
 GridLines→{{peakl,peakr,peak},{peakbottom}},
 Epilog→{Opacity[0.5,Blue],Point[baseline]},*)
 GridLinesStyle → Directive[Orange, Dashed]]
```
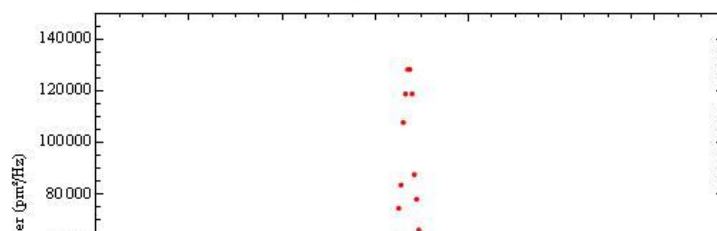
Fit the peak data to find the Q factor

```
(*f[ω_, ωr_, A0_, Aw_, Q_]:=Aw+ (A0 ω⁴)/((ω²-ωr²)²+(ω²ωr²)/Q²)

fitpeak=FindFit[spike,f[ω, ωr, A0, Aw, Q], {{ωr, peak}, A0, {Aw,0.25}, {Q,350}},
     ω,MaxIterations→50000] Original form, just in case.*)
```

$$f[\omega\_, \omega r\_, A0\_, Aw\_, Q\_] := Aw + \frac{A0\ \omega r^4}{\left(\omega^2 - \omega r^2\right)^2 + \frac{\omega^2\ \omega r^2}{Q^2}}$$

```
fitpeak = FindFit[spike, f[ω, ωr, A0, Aw, Q],
    {{ωr, peak}, A0, {Aw, 0.25}, {Q, 350}}, ω, MaxIterations → 50 000];
Print[{"= Q" Q /. fitpeak, "kHz = ωr" ωr /. fitpeak}]
```

{636.992 = Q, 266.705 kHz = ωr}

Appendix B: Mathematica code for analysis of force curves

```
SetDirectory["Directory path with exported .txt files goes here"];
plotsize=400;
Needs["PlotLegends`"];
dataFiles=FileNames["*.txt"];
(*Get all the file names in the directory for importing.*)

dataNumberStr=StringTake[dataFiles,{20,22}];(*Take only the digits that increment as file
number changes*)

dataNumberExp=ToExpression[dataNumberStr];(*These are integers*)

xpos=Riffle[Reverse[Table[i,{i,0,IntegerPart[Length[dataFiles]/2]*10,10}]],Reverse[Table[
i,{i,0,IntegerPart[Length[dataFiles]/2]*10,10}]]];

(*Fills a dummy table the same length as many force curve files were found, in steps of 10 nm
for the position.*)

(*This for loops runs through the body of the loop for all of the data files found in the directory*)
For[file=1;,file<Length[xpos]+1,file++;,

SetDirectory["Filepath goes here"];

Clear[raw];

raw= Drop[Import["Standardized file name prefix"<>dataNumberStr[[file]]<>".000.txt",
"TSV"], 904, -1];

dc0e2=Map[{#[[3]],#[[5]]}&,raw];
ze=Select[dc0e2[[All,1]],NumberQ];
dc0e=Select[dc0e2[[All,2]],NumberQ];

dc0r2=Map[{#[[4]],#[[6]]}&,raw];
zr=Select[dc0r2[[All,1]],NumberQ];
zr=Reverse[zr];
dc0r=Select[dc0r2[[All,2]],NumberQ];
dc0r=Reverse[dc0r];
ze=Map[#+(zr[[-1]]-ze[[-1]])&,ze];

(*The 3rd (extend) and 4th (retract) columns of the data files are the calculated ramp, 11th and
12th are the height sensor data, the 5th and 6th are deflection.*)

dl=Length[dc0e]-Length[dc0r];
```

```
dz=Length[ze]-Length[zr];
```

(*Adjust the lengths of the extend and retract lists to match.*)

```
If[dl>0 ,
dc0e=Drop[dc0e,Abs[dl]],
dc0r=Drop[dc0r,Abs[dl]]
];
If[dz>0 ,
ze=Drop[ze,Abs[dl]],
zr=Drop[zr,Abs[dl]]
];
```
(*Shift the deflection baseline to 0 by subtracting the average of the first 1/3 data points from the entire list.*)

```
basee=Mean[Take[dc0e,IntegerPart[Length[dc0e]/3]]];

dce=dc0e-basee;

dcr=dc0r-basee;
```

(*Calculate nanorod deflection dn = z - dc*)

```
dne=ze-dce;
dnr=zr-dcr;
```

(*Multiply the cantilever deflection dc times the force constant of the cantilever to get the force data, then make the list of x-y coordinates for plotting.*)

```
kc=33.74;
forcee=dce*kc(*calculate the cantilever force by F = kc dc*);
forcer=dcr*kc;
fdce=Partition[Riffle[ze,dce],2];
fdcr=Partition[Riffle[zr,dcr],2];

fdne=Partition[Riffle[ze,dne],2];
fdnr=Partition[Riffle[zr,dnr],2];
teste=MovingAverage[Reverse[dce],7];
testr=MovingAverage[Reverse[dcr],7];

cpe=TakeWhile[teste,#>=0&]//Length;
cpr=TakeWhile[testr,#>=0&]//Length;

contacte=Length[dce]-cpe;
contactr=Length[dcr]-cpr;
```

If[contacte<IntegerPart[Length[fdce]/3],contacte=contactr];
If[contactr<IntegerPart[Length[fdcr]/3],contactr=contacte];

(*Shorten the deflection of cantilever, nanorod and force lists to only after the contact point, and zero the nanorod deflection with the first point being 0.*)

aclengthe=Length[ze]-contacte;
aclengthr=Length[zr]-contactr;

dneac0=Take[dne,-aclengthe];
dnrac0=Take[dnr,-aclengthr];

dceac=Take[dce,-aclengthe];
dcrac=Take[dcr,-aclengthr];

forceeac=Take[forcee,-aclengthe];
forcerac=Take[forcer,-aclengthr];

dneac=dneac0[[All]]-dneac0[[1]];
dnrac=dnrac0[[All]]-dnrac0[[1]];

(*This riffles the lists together,then partition them into groups of 2. ie;{{x1,x2,x3},{y1,y2,y3}}->{{x1,y1},{x2,y2},{x3,y3}}*)

fvdce=Partition[Riffle[dceac,forceeac],2]; (*make an x,y list of the force vs cantilever defl for plotting*)
fvdcr=Partition[Riffle[dcrac,forcerac],2];

fvdnce0=Partition[Riffle[dneac,forceeac],2];(*make an x,y list of the force vs n-c defl for plotting *)
fvdncr0=Partition[Riffle[dnrac,forcerac],2];

(*Find the first position in the force vs net deflection list where the y value is positive and drop all elements before that one*)
fvdnce=Drop[fvdnce0, First[First[Position[fvdnce0,First[Select[fvdnce0[[All,2]],#>=0&] (*Sel*)] (*First*)](*Pos*)] (*First*)] (*First*)](*Drop*);
fvdncr=Drop[fvdncr0, First[First[Position[fvdncr0,First[Select[fvdncr0[[All,2]],#>=0&] (*Sel*)] (*First*)](*Pos*)] (*First*)](*First*)](*Drop*);

mindce = {fdce[[contacte, 1]], fdce[[contacte, 2]]};
mindcr = {fdcr[[contactr, 1]], fdcr[[contactr, 2]]};

mindne = {fdne[[contacte, 1]], fdne[[contacte, 2]]};
mindnr = {fdnr[[contactr, 1]], fdnr[[contactr, 2]]};

cantdefplot=ListPlot[{fdce,fdcr},

```mathematica
PlotRange->{{0,100},{-5,10}},
PlotLabel->"Cantilever Deflection vs Z piezo height",
PlotLegend->{"Extend","Retract"},
LegendPosition->{-0.8,0.25},
LegendSize->0.4,
Frame->True,
FrameStyle-> Directive[Black],
FrameLabel->{"Z Piezo (nm)","Cantilever Deflection (nm)"},
ImageSize->plotsize,
Epilog->{PointSize[Large],Point[{mindce,mindcr}]},
LegendShadow->False
];

SetDirectory["exported"];

Export[ToString[dataNumberStr[[file]]] <>"def.jpeg",cantdefplot,"JPEG"];

knelmf=LinearModelFit[fvdnce,x,x];
kne0=LinearModelFit[fvdnce,x,x][[1,2,2]];(*Extracts the slope of the linear fit and assigns it to a
variable for exporting.*)

knrlmf=LinearModelFit[fvdncr,x,x];
knr0=LinearModelFit[fvdncr,x,x][[1,2,2]];

kne=Abs[((kne0)^-1-(kc)^-1)^-1];
knr=Abs[((knr0)^-1-(kc)^-1)^-1];

forceplot=ListPlot[{fvdnce,fvdncr},
PlotRange->{{0,15},{0,300}},
ImageSize->plotsize];
fitplot=Plot[{knelmf[x],knrlmf[x]},{x,0,15},
PlotRange->{{0,15},{0,300}},
ImageSize->plotsize];

forcePlotExport=Graphics[{forceplot[[1]],fitplot[[1,1,3]],fitplot[[1,1,4]]},Axes-
>True,AspectRatio->0.75,Frame->True,FrameLabel->{"Nanorod Deflection (nm)","Force
(nN)"},PlotLabel->"Force vs. Nanorod Deflection"];

Export[ToString[dataNumberStr[[file]]]<>"fit.jpeg",forcePlotExport,
"JPEG"];

ToString[dataNumberStr[[file]]] <>", "<>ToString[kne]<>", "<>ToString[knr]<> ",
"<>ToString[xpos[[file]]]>>>"rod5.txt";
]
```